nature physics

Article

https://doi.org/10.1038/s41567-022-01755-0

Rigid tumours contain soft cancer cells

Received: 20 December 2016

Accepted: 15 August 2022

Published online: 29 September 2022

Check for updates

Thomas Fuhs[1,14], Franziska Wetzel[1,14], Anatol W. Fritsch[1,2,14], Xinzhi Li[3,14], Roland Stange[1], Steve Pawlizak[1], Tobias R. Kießling[1], Erik Morawetz[1], Steffen Grosser[1], Frank Sauer[1], Jürgen Lippoldt[1], Frederic Renner[1], Sabrina Friebe[1,4], Mareike Zink[1], Klaus Bendrat[5,6], Jürgen Braun[7], Maja H. Oktay[8], John Condeelis[9], Susanne Briest[10], Benjamin Wolf[10], Lars-Christian Horn[11], Michael Höckel[10], Bahriye Aktas[10], M. Cristina Marchetti[12], M. Lisa Manning[13], Axel Niendorf[5], Dapeng Bi[3] and Josef A. Käs[1] ✉

Palpation utilizes the fact that solid breast tumours are stiffer than the surrounding tissue. However, cancer cells tend to soften, which may enhance their ability to squeeze through dense tissue. This apparent paradox proposes two contradicting hypotheses: either softness emerges from adaptation to the tumour's microenvironment or soft cancer cells are already present inside a rigid primary tumour mass giving rise to cancer cell motility. We investigate primary tumour explants from patients with breast and cervix carcinomas on multiple length scales. We find that primary tumours are highly heterogeneous in their mechanical properties on all scales from the tissue level down to individual cells. This results in a broad rigidity distribution—from very stiff cells to cells softer than those found in healthy tissue—that is shifted towards a higher fraction of softer cells. Atomic-force-microscopy-based tissue rheology reveals that islands of rigid cells are surrounded by soft cells. The tracking of vital cells confirms the coexistence of jammed and unjammed areas in tumour explants. Despite the absence of a percolated backbone of stiff cells and a large fraction of unjammed, motile cells, cancer cell clusters show a heterogeneous solid behaviour with a finite elastic modulus providing mechanical stability.

Early on, tumour biology recognized that cancer cells undergo dedifferentiation towards a more disordered and thus softer cytoskeleton[1]. Evidence for soft cells already inside primary tumours is, however, only circumstantial and cell lines differ from clinical samples[2–5]. Cell softening is associated with the downregulation of keratin after partial or complete epithelial–mesenchymal transition[6,7]; these cells migrate more efficiently through dense environments[8], until nuclear jamming hinders further movement[9,10]. For metastatic cells extracted from extracellular fluids such as pleural effusions, softness correlates with clinical pathology[5]. Similarly, cytobrushes indicate cancer cell softening in oral

[1]Soft Matter Physics Division, Leipzig University, Leipzig, Germany. [2]Max Planck Institute of Molecular Cell Biology and Genetics (MPI-CBG), Dresden, Germany. [3]Department of Physics, Northeastern University, Boston, MA, USA. [4]Leibniz Institute of Surface Engineering and Surface Physics, University of Leipzig, Leipzig, Germany. [5]Pathologie Hamburg-West, Hamburg, Germany. [6]Institute for Biochemistry and Molecular Cell Biology, University Hospital Hamburg-Eppendorf, Hamburg, Germany. [7]Institute of Medical Informatics, Charité—Universitätsmedizin Berlin, Berlin, Germany. [8]Department of Pathology, Albert Einstein College of Medicine and Montefiore Medical Center, Bronx, NY, USA. [9]Gruss Lipper Biophotonics Center and Integrated Imaging Program, Albert Einstein College of Medicine, Bronx, NY, USA. [10]Department of Gynecology, Women's and Children's Center, University Hospital Leipzig, Leipzig, Germany. [11]Division of Breast, Urogenital and Perinatal Pathology, University Hospital Leipzig, Leipzig, Germany. [12]Department of Physics, University of California, Santa Barbara, CA, USA. [13]Department of Physics, Syracuse University, Syracuse, NY, USA. [14]These authors contributed equally: Thomas Fuhs, Franziska Wetzel, Anatol W. Fritsch, Xinzhi Li. ✉e-mail: jkaes@physik.uni-leipzig.de

cancer[11]. In contrast, circulating breast cancer cells are slightly stiffer than the surrounding white blood cells[12]. Fine-needle aspirations of breast tumours show that solid tumours contain well-defined soft regions[13,14], although it remains unclear if these soft areas are composed of cancer cells or extracellular matrix (ECM).

Our recent research indicates that the fluid or solid behaviour of cancer cell clusters in breast and cervical tumours is modulated by cell unjamming[15]. Cell proliferation requires a cell cluster resistant enough to divide against a typically firm surrounding stroma[16,17], yet proliferation fluidizes tissues[18,19]. Cancer cell spheroids can spread like a fluid droplet[20], and yet their shapes and sorting behaviours are not solely governed by surface tension[21]. Many cell aggregates exhibit features of glassiness or jamming, suggesting the mechanical impact of solid–fluid transitions on tissue bulk behaviour[22,23]. Because fluid-like and solid-like tissues have different mechanisms for proliferation[24], migration, self-organization and cohesion (that is, cancer cell escape)[25], these uncertainties prevent us from fully understanding the initial metastatic cascade.

Nonetheless, a breast tumour is undoubtedly a rigid mass, as already stated in the ancient Egyptian medical text Ebers Papyrus. Neoplastic tissue, composed of cancer cell clusters surrounded by enhanced, stiff and often fibrotic stroma, appears as a rigid mass[26] with respect to the healthy surrounding tissue. Pathologists use excessive ECM deposition as a marker for poor prognosis, since it is a strong tumour promoter[27,28]. Tumour progression seems to simultaneously require rigid and soft properties of cancerous tissue and individual cancer cells. This apparent paradox, as discussed recently[17], is solved by us by unique multiscale mechanical measurements on patient-derived tumour explants.

Moreover, cancer cells are highly mechanosensitive and mechanically adapt to their microenvironment. Mechanical changes may be directly caused through mechanosensitive responses of the cytoskeleton or through expression changes by cellular mechanotransduction[29–31]. This may cause cell stiffening after the cancer cell has left the tumour cell mass into the stiff ECM. Moreover, fluid unjammed cancer cell clusters may induce cancer cell softening or softening may be the cause of unjamming. The question remains if mechanical changes already start in the tumour mass or rather occur only when the cells leave into the stroma.

Multiscale tumour mechanics

Starting on the bulk-tissue level, we quantified macroscopic viscoelasticity with tabletop magnetic resonance elastography (MRE)[32–34] on centimetre-sized vital tumour explants, from cervical and mammary carcinomas (Figs. 1 and 2). Soft tissues and cells often exhibit a distinctive power-law viscoelastic response[35], described by the complex shear modulus derived from the fractional Maxwell model. We extract the stiffness/elastic resistance (μ) and its power-law exponent (α) as a measure for fluidity/dissipation. The cells and tissues are highly complex compound materials, and no analytic constitutive model exists to describe their multiscale mechanical behaviour. Thus, mechanical constants measured with diverse techniques on different scales cannot be quantitatively compared[36]. Nevertheless, the measured mechanical behaviours can be compared and correlated.

The MRE data confirm the medical practice that breast cancer can be identified by palpation; breast tumour explants ($n = 5$) with a median mechanical resistance of $\mu_{BC} = (2.9 \pm 1.9) \times 10^5$ Pa are clearly ($p = 0.021$, Kolmogorov–Smirnov (KS) test) stiffer than healthy breast tissue with $\mu_{BN} = (163 \pm 77)$ Pa ($n = 3$), whereas the fluidity is similar (Fig. 1b). In the tumour explants, the fibrotic stroma may contribute to an increase in stiffness, whereas healthy epithelial breast tissue is surrounded by connective tissue and very soft fat tissue, which may dominate the averaged bulk stiffness measured by MRE.

In contrast, for the cervix samples, tumours $(4.4 \pm 1.4) \times 10^4$ Pa are not significantly ($p = 0.53$, KS test) stiffer than healthy tissue ($(1.4 \pm 1.3) \times 10^5$ Pa) and have similar fluidity (for both, $n = 4$). The cervical epithelium is primarily surrounded by rigid connective tissue and smooth muscle cells. For effective cancer cell proliferation, it is sufficient if the tumour just matches or slightly exceeds the resistance of the surrounding microenvironment[16]. Moreover, cervical tissue is highly active showing functional and structural changes, for example, during the menstrual cycle, which is reflected in variably altered viscoelastic properties[37]. This demonstrates that carcinomas do not have to be drastically stiffer than the healthy surrounding tissue[38].

With the atomic force microscopy (AFM) technique, we measured the elasticity maps of the same live tumour explants with cellular resolution to capture the local, heterogeneous distribution of stiffness. We see a log-normal distribution in stiffness (Fig. 1e), also seen in single-cell AFM measurements[39,40]. For breast cancer, we observe a stiffening in the median Young's Modulus from $E_{BN} = 132$ Pa ($n = 16$) to $E_{BC} = 288$ Pa ($n = 13$) moving from healthy to cancerous tissue. In the cervix, we see a drop in median stiffness from $E_{CN} = 570$ Pa ($n = 5$) for healthy cervix to $E_{CC} = 385$ Pa ($n = 7$) in cervical cancer. These values integrate over the differences between stroma and cancer cell clusters. Within the cancer cell clusters, we observe smaller stiff regions surrounded by softer cells, both spanning several hundreds of micrometres (Fig. 1c). The regions of soft cells are percolated within the observed sections. Moreover, the stiff regions remain in isolated areas. Since we have only sections of the tumour, it remains unclear whether the rigid regions are percolated or remain islands in three dimensions. The soft and stiff regions within the cell clusters show a solid behaviour with finite elastic moduli. This mechanically stable behaviour permits the understanding that fibrotic stroma does not solely contribute to the rigidity of a solid tumour.

Carcinomas contain cells that are softer than healthy cells

Suspended cells lose all stimuli from their microenvironment and enter an unperturbed ground state, so that changes must be due to expression changes. This ground state was characterized in step-stress experiments with an optical stretcher (OS)[41] (Fig. 3). For cervical tumours, neighbouring normal epithelial tissue was used as a reference. For breast cancer, it was benign lesions (fibroadenoma, FA) and primary human mammary epithelial cells (HMEpC) from breast reductions. All the samples were in culture for a short time, as primary cells soften with time in culture (Extended Data Fig. 1). As the HMEpC controls were in culture longer than the tumour samples, the observed differences underestimate the relative softening of cancer cells.

The relative deformation of measured cells also follows a log-normal distribution. From the cumulative distribution of 13 breast cancer samples ($n = 6{,}526$), compared with two FA samples ($n = 186$) and one HMEpC sample ($n = 358$), we find that the breast cancer cells are the softest with a median relative deformation of $MD_{BC} = 0.024$ (FA cells, $MD_{FA} = 0.015$; healthy cells, $HMEpCMD_{HMEpC} = 0.018$) (Fig. 3 and Extended Data Fig. 2). All the differences are significant.

An increase in soft cancer cells with respect to healthy cells characterizes both breast and cervical tumours (Extended Data Table 1). The cells from tumours are more heterogeneous, that is, they display a broader log-normal distribution, with a large fraction of cells that are just as stiff as those in normal tissues. Primary carcinoma contains soft as well as rigid cells, which could stem from cancer deregulation or the broad spectrum of epithelial and mesenchymal states may cause the variability in cytoskeletal expression that cause this heterogeneous behaviour. In cancer cell clusters, these cells separate in regions of soft and rigid cells, as shown by our AFM measurements. The stiffening of breast tissue felt by palpation can be attributed to the different compositions of healthy and cancerous breast tissue, as soft fat cells get replaced by large volumes of cancer cells. These cancer cells are a lot stiffer than fat cells, even if they are softer than the healthy epithelial cells that they originate from in the first place.

https://doi.org/10.1038/s41567-022-01755-0

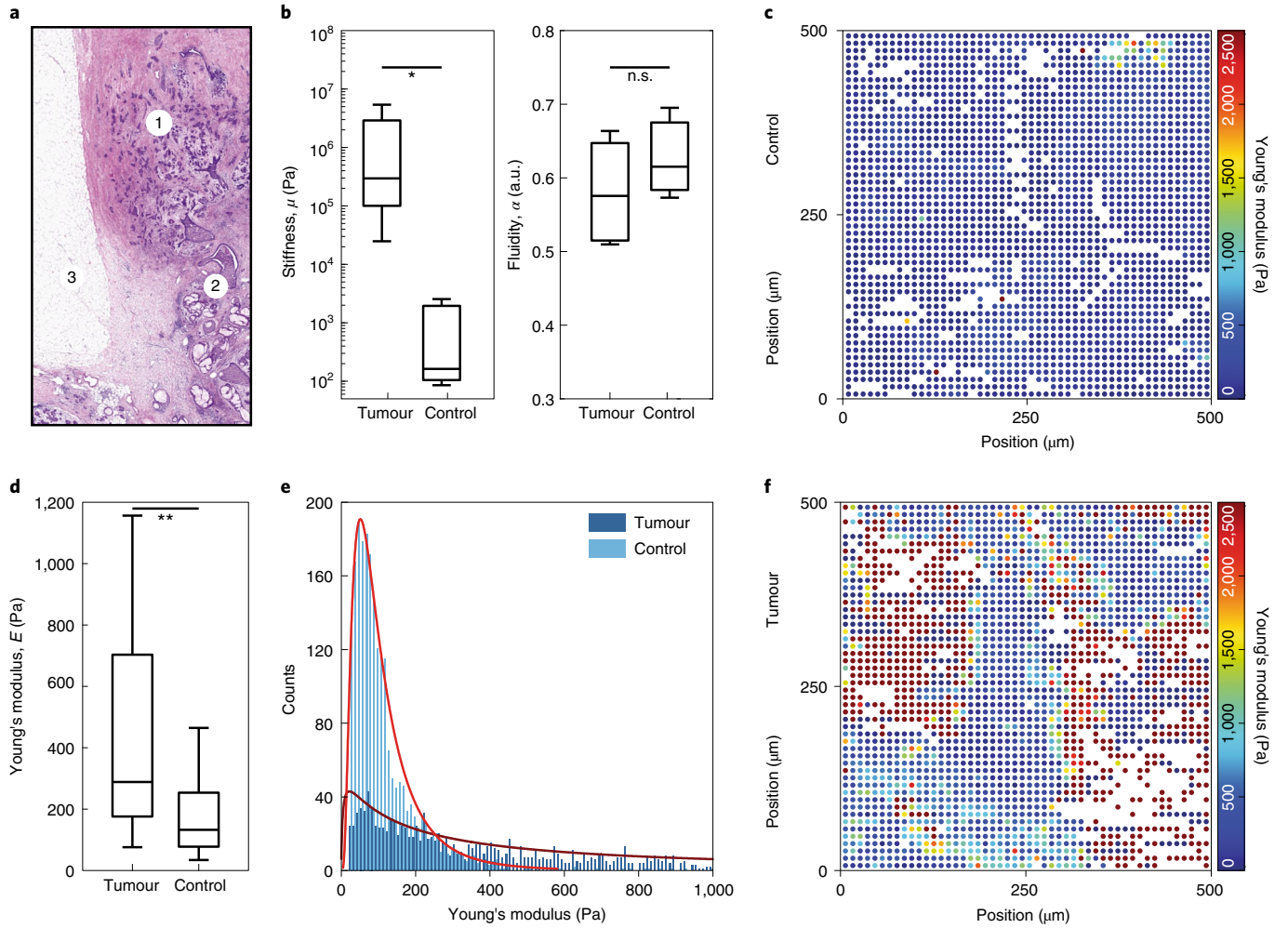

Fig. 1 | Viscoelasticity of breast cancer tissue. a, Haematoxylin and eosin stain of invasive breast cancer growth: regions of desmoplastic reaction (1), intraductal tumour growth (2) and fatty tissue (3) can be identified. **b**, MRE of breast tumours. Centimetre-sized vital pieces of primary breast tumours ($n = 5$) and healthy breast tissue ($n = 3$) were measured. The bulk stiffness μ of tumours is higher compared with healthy tissue, as expected from palpation ($p = 0.021$, KS test), and the difference in fluidity α is not significant. **c**,**f**, AFM maps of local tissue elasticity for breast tumour and healthy breast tissue. Tissue elasticity maps measured for 0.5×0.5 mm^2 areas in vital tissue explants with 10 μm resolution reveal domains of several hundreds of micrometres in size with distinctively higher or lower local elasticity leading to a heterogeneous structure. **d**, Median breast tissue stiffness; the median Young's modulus rises from $E_{BN} = 132$ Pa ($n = 16$) to $E_{BC} = 288$ Pa ($n = 13$) moving from healthy to cancerous tissue ($p < 0.01$, MWU test). **e**, Distribution of local Young's moduli of breast cancer tissue (dark blue) and control tissue (light blue) from the maps shown in **c** and **f**. Both tissues show a log-normal distribution in stiffness (red fit lines), with the tumour showing a much wider, heterogeneous distribution in stiffness. The box plots show quartiles 1, 2 and 3 (box) and 5%/95% (whiskers); n.s., not significant; $^*p < 0.05$, $^{**}p < 0.01$.

Cancer cell unjamming modulates stiffness of cell clusters

In tumour explants, we have found unjammed as well as jammed regions by vital cell tracking. To understand how such regions affect the global tumour behaviour, we use cell spheroids to illustrate the mechanical properties of jammed and unjammed tissues. We have recently shown that MDA-MB-436 spheroids, a model for breast cancer, consist of unjammed cells that can move, whereas MCF-10A spheroids, a model for epithelial cells, consist of jammed, non-moving cells[15]. Spheroid fusion experiments demonstrate that spheroids with motile cells behave like a fluid and jammed cell clusters have properties of an amorphous solid[15]. This exemplifies the fact that tissue fluidity, as an emergent collective cell behaviour, is a key modulator of tissue stiffness. We performed force–indentation experiments on spheroids with an AFM instrument. MCF-10A spheroids have an elastic modulus of 88(±63) Pa compared with 135(±38) Pa for single cells. MDB-MB-436 spheroids dropped from a single-cell elastic modulus of 570(±300) Pa to 111(±72) Pa for spheroids (Fig. 4). The motile cells in MDB-MB-436 spheroids oppose much less external loads compared with individual cells. The jammed MCF-10A spheroids also lose some of their individual strength but only 36% compared with the 80% value of MDA-MB-436. We tracked the fusion of nine pairs of MCF-10A spheroids and ten pairs of MDA-MB-436 spheroids. The fusion progress rate—measured as $\Delta(\cos\theta)/\Delta t$—between 24 and 36 h after fusion start, was significantly different between the two fusion experiments. Qualitatively, MCF-10A fusions virtually arrest, in contrast to the ongoing MDA-MB-436 fusions (Fig. 4). Together with the AFM measurements, this establishes the fact that tissue fluidity rather than direct individual cell stiffness impacts the mechanical stability of cell clusters. Single-cell stiffness may be more of a determinant of tissue fluidity. Already, the two cell lines show broad log-normal distributions for their cell stiffness. Furthermore, the primary tissue samples are even more heterogeneous. Our AFM-based cell elasticity maps of cervix and breast carcinoma display rigid and soft regions. The soft areas are unjammed and the rigid ones are jammed. If the rigid cells do not form a percolated backbone, how can the tissue maintain a mechanically stable behaviour with a finite elastic modulus?

https://doi.org/10.1038/s41567-022-01755-0

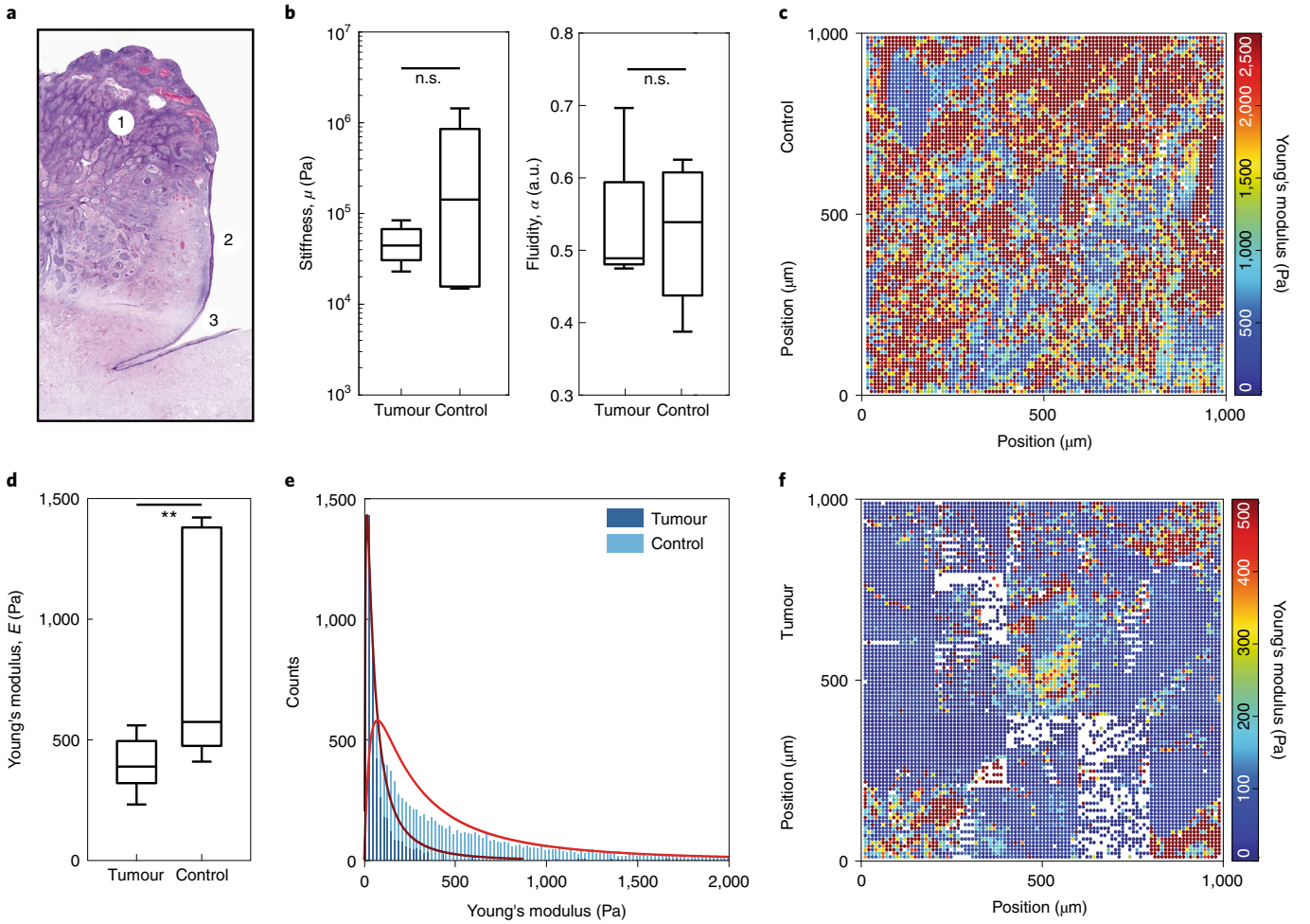

Fig. 2 | Viscoelasticity of cervix cancer tissue. a, Haematoxylin and eosin stain of squamous cell carcinoma of the uterine cervix; the tumour (1) is confined to the cervix. The vaginal cuff (3) and ectocervix (2) are not affected. **b**, MRE of cervical tumours. Centimetre-sized pieces of vital primary tumour explants of cervical tumours ($n = 4$) and healthy cervix tissue ($n = 4$) were measured. On the bulk-tissue level, tumours are similar compared with healthy tissue. The tumour is not significantly stiffer or more fluid than the surrounding tissue (n.s.; KS test). **c**,**f**, AFM-based map of local tissue elasticity of cervix carcinoma and healthy control tissue. Tissue elasticity measured for patches of $1 \times 1\,mm^2$ with 10 μm resolution from vital tissue explants reveals that the cancer cell clusters are heterogeneously divided into domains of several hundreds of micrometres with high or low local elastic strength. **d**, Median cervix tissue stiffness; in the cervix, we see a drop in median stiffness from $E_{CN} = 570$ Pa ($n = 5$) for healthy cervix to $E_{CC} = 385$ Pa ($n = 7$) in cervical cancer ($p < 0.01$, MWU test). **e**, Histogram of the distribution of local Young's moduli from AFM measurements of cervix cancer tissue and control tissue, from the maps shown in **c** and **f**. Both tissues show a log-normal distribution in stiffness (red fit lines), with the tumour only displaying softer cells than the cells from the healthy tissue. The box plots show quartiles 1, 2 and 3 (box) and 5%/95% (whiskers). n.s., not significant; $^{**}p < 0.01$.

Regions of rigid cells surrounded by soft, motile cells

We used the measured stiffness distribution from patient samples and a vertex-based model[42,43] used for the unjamming transition[44–48] to disentangle the influence of a stiff and soft fraction of cancer cells on tissue mechanics (Fig. 5)[49]. Our qualitative simulations show—in a reductionist situation only—how the interplay of soft and rigid cells can assume different states of tissue fluidity depending on the distribution of soft and rigid cancer cells. For a tissue of mechanically homogeneous cells, the collective fluidity is controlled by the cell shape index P_0, which describes the interaction between cellular cortical tension (that is, effective cell stiffness) and cell adhesion. Cells with large tension tend towards a stiff, round shape, whereas when it is low, cells tend towards a softer, elongated shape[15,50,51]. Thus, round, stiff cells with a shape parameter smaller than the critical P_0 collectively assume the state of an amorphous, jammed solid, whereas elongated, soft cells with a larger shape parameter are motile in a cooperative fluid, unjammed state.

We have stratified the fraction of soft and stiff cancer cells in our model[49] based on the measured stiffness distributions, since the elastic modulus of a single cell is linearly proportional to P_0 for small deformations[52]. Since carcinoma shows a mixed epithelial and mesenchymal phenotype[7] and different cadherins can bind to each other[53], we assume that differences in P_0 between the cancer cells are predominantly caused by changes in the cancer cell's cortical tension and differences in cell–cell adhesion are less important. Cancer cell unjamming is further modulated by mechanical effects of the nucleus[15] and other effects. We have recently identified the mechanism of 'second-order rigidity' as a key driver[54,55], which works in the same fashion in two and three dimensions. Since all our results are verified by experimental data, we visualized the mechanism in a qualitative two-dimensional model for clarifying how mechanical heterogeneity influences the tissue mechanics. In our model, the mechanical bulk property of the cell collective is determined by computing the shear modulus G (ref. [56]). In terms of mechanical stability, G is finite in a fully jammed, solid tissue, but vanishes in a completely unjammed, fluid one.

We computed G as a function of the mean and standard deviation (s.d.) of P_0 and found three distinct mechanical phases (Fig. 5a): a fully unjammed (fluid) phase where the shear modulus of the tissue

https://doi.org/10.1038/s41567-022-01755-0

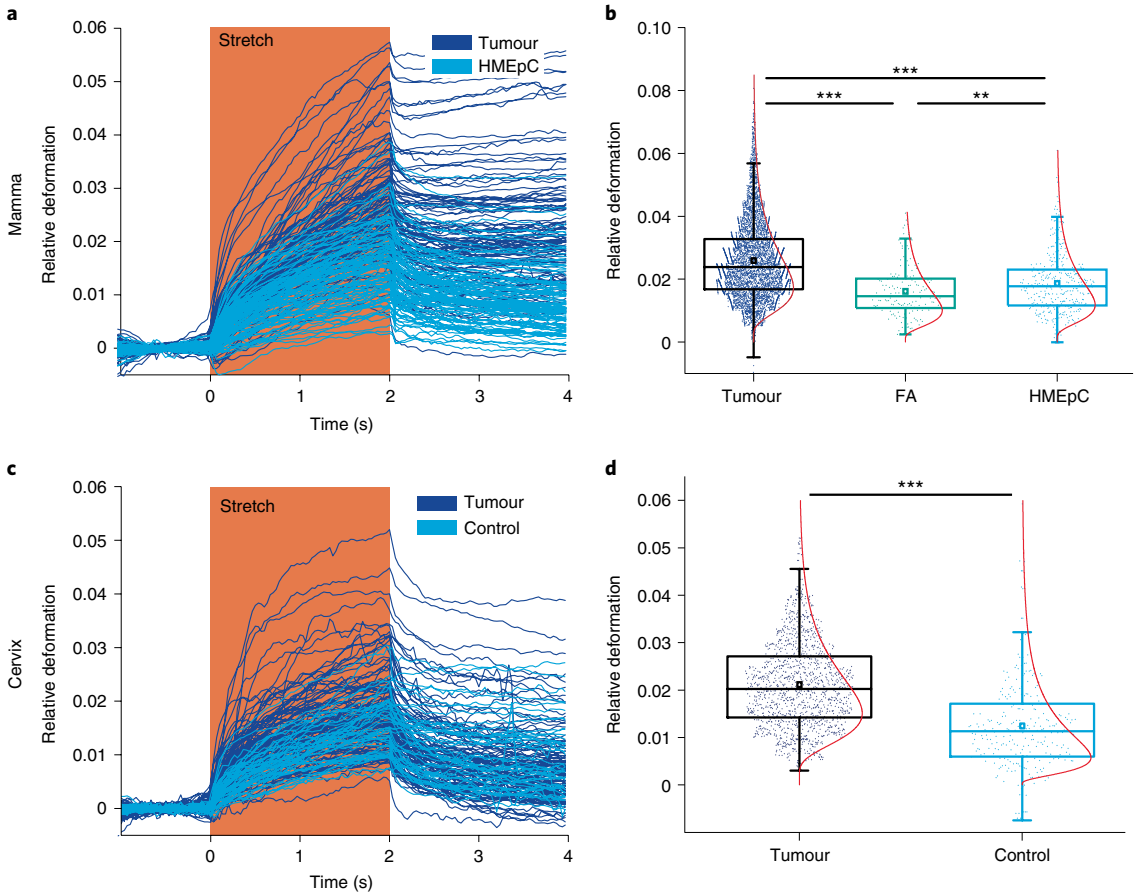

Fig. 3 | Single-cell mechanics of carcinomas. a, Relative deformation and relaxation curves of single measured cells from a breast carcinoma (tumour, $n = 613$) compared with primary HMEpC cells from healthy epithelial breast tissue from breast reductions ($n = 358$). The cells are deformed by the laser during the 2 s stretch period (orange band) and relax afterwards. **b**, Cumulative distribution over 13 breast cancer samples ($n = 6{,}526$), compared with the two FA samples ($n = 186$) and one HMEpC sample ($n = 358$). A log-normal distribution was successfully fitted (red fit lines). The distribution is clearly shifted towards softer cancer cells. Nevertheless, the extreme width of the distribution means that even stiff cancer cells exist within the tumour mass. **c**, Relative deformation and relaxation behaviour of single cells from a cervical carcinoma ($n = 111$) compared with normal cervical epithelial ($n = 38$) tissue from the same patient. The stretching time is 2 s (orange band). **d**, Cumulative distribution over four pairs of cervix samples ($n_{CT} = 1{,}481$, $n_{CN} = 262$) (**$p < 0.01$, ***$p < 0.001$, MWU test). A log-normal distribution fits the data very well (red fit lines). The cancer-cell softening effect visible by the shift in distribution towards larger relative deformations is for the cervix carcinoma—even more pronounced than breast tumours. The box plots show quartiles 1, 2 and 3 (box); 5%/95% (whiskers); and mean (small square).

remained zero; a partially jammed, heterogeneous phase where tension percolation gives a finite bulk stiffness; and a solid phase. This tissue classification is also well founded in our AFM and OS data, independent of the simulations. The edge tensions have been calculated based on P_0 values of two neighbouring cells (Methods). Stiff cells ($P_0 < 3.812$) form the jammed regions (Fig. 4b), whereas soft cells are responsible for fluid regions. In the heterogeneous solid phase, the tension network self-organizes into a percolated structure, yet the rigid, jammed cells do not percolate. This suggests that a small fraction of jammed islands in a fluid sea, as observed in our patient-derived tumour explants, are sufficient to give rise to a finite shear modulus. In the fully solid phase, both tension and stiff cells form percolating networks. In our AFM data (Fig. 1), we find—for tumours—the same stiff islands surrounded by soft cells with a finite bulk modulus analogous to the heterogeneous solid state in our simulations. In the healthy tissue samples, we find a more homogeneous stiffness distribution, suggesting a more solid-like behaviour.

The solid heterogeneous phase is clearly determined by the fraction of rigid cells in the tissue, f_r (Methods). The pure fluid phase only exists for $f_r < 0.24$, also visible when plotting the shear modulus over f_r (Fig. 5c). The heterogeneous solid spans $0.24 < f_r < 0.48$, and the fully solid phase corresponds to $f_r > 0.48$. The dependence of tissue mechanics[49] on f_r reveals that tumour heterogeneity, that is, variance $\sigma(P_0)$, fosters the rigidification of a tumour, which can be seen by the positive slope of the phase boundaries (Fig. 5a). This suggests that a tissue can rigidify with increasing cellular heterogeneity, as evident in the widening of the stiffness distribution of single cancer cells.

With further simplified dynamical vertex model simulations where every cell experiences an active propulsive force[57] (Methods), we elucidate the effect of heterogeneity and the fraction of rigid cells on tissue fluidity. The long-time migration behaviour is described by the self-diffusivity D_{eff} (ref. [58]). The fluid phase is characterized by a finite value of D_{eff}, and D_{eff} becomes vanishingly small (Methods) as the solid state is approached at $f_r = 0.48$. This suggests that the heterogeneous solid ($0.24 < f_r < 0.48$) is jammed with respect to small perturbations but can be fluidized when subject to a large propulsive force. In the solid phase ($f_r > 0.48$), the cells are jammed and diffusive motion is completely hindered due to the contact percolation of rigid cells.

Our patient-derived stiffness data positions within the phase diagram with respect to the fraction of rigid cells f_r confirm the classification by looking at the spatial stiffness maps measured by AFM (Methods). This permits the categorization of breast and cervical tumour samples with respect to our phase diagram (Fig. 5e). We find that breast and cervical cancer samples are located within the heterogeneous solid phase permitting a large fraction of unjammed, motile

https://doi.org/10.1038/s41567-022-01755-0

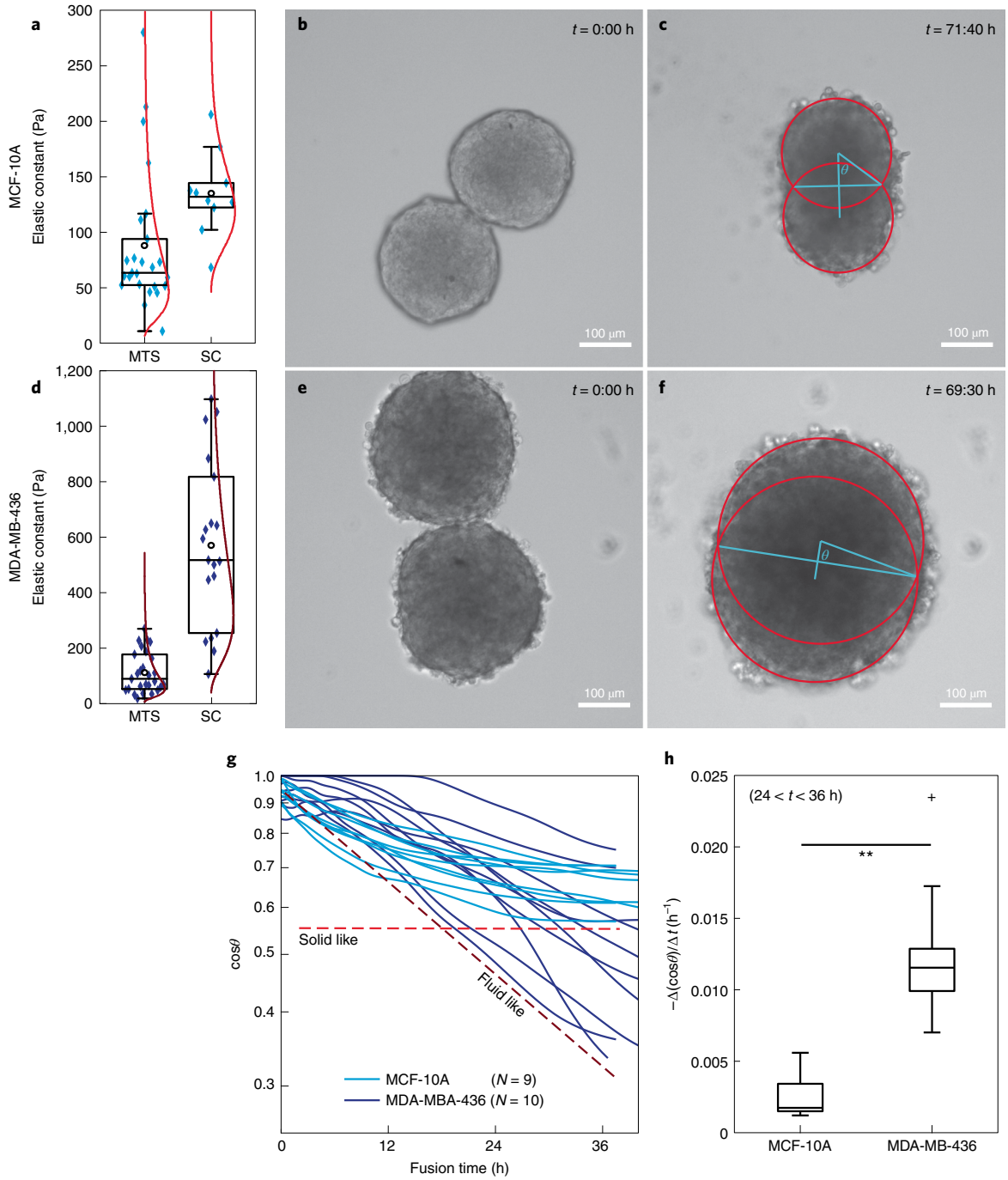

Fig. 4 | Mechanics and fusion of multicellular spheroids. a, Elastic modulus of MCF-10A (representing healthy breast epithelium) spheroid compared with single cells measured by AFM indentation experiments based on the Hertz model. The spheroids formed by MCF-10A cells soften to 88 Pa in contrast to 135 Pa for single cells; the fits (red) are log-normal fits. **b**,**c**, MCF-10A spheroids do not fuse completely; the fusion arrests at smaller θ ($\theta \approx 50°$). **d**, Spheroids formed by MDA-MB-436 (malignant breast cancer cells) soften by a factor of 5 from 570 Pa (single cells) to 111 Pa (MTS); the fits (red) are log-normal fits. The cells freely move within the cluster. This fluid behaviour leads to significant softening of the spheroid. **e**,**f**, MDA-MB-436 spheroids fuse almost completely and the angle θ between the line connecting the centres of the spheroids (red circle fit) and the radius to the contact point (blue lines) approaches 90° ($\theta \approx 80°$). **g**, Individual tracks of θ over time for MCF-10A and MDA-MB-436. **h**, Fusion progress rate, as measured by $\Delta(\cos\theta)/\Delta t$ between 24 and 36 h after fusion start, was significantly different between fusion experiments ($p < 0.001$, KS test). The most pronounced difference between the samples, however, was of a rather qualitative nature. MCF-10A fusions virtually arrest, in contrast to the ongoing MDA-MB-436 fusions (dashed lines for guidance). The box plots show quartiles 1, 2 and 3 (box); 5%/95% (whiskers); and mean (circle). All the data points are plotted in **a** and **d** (blue diamonds); $^{**}p < 0.01$.

cells, whereas healthy cells from breast reductions, cells from healthy cervix tissue and benign FAs are in the solid, jammed phase. Here the log-normal distributions measured with OS and the spatial distributions measured with AFM lead to the same result concerning the classification of tissue in the phase diagram.

The spatial organization of cancer cells in clusters with soft, motile and rigid, jammed regions within a tumour causes the counterintuitive result that many soft cells can exist within the solid mass without destroying its mechanical stability as a solid that resists the microenvironment. Even where no backbone of stiff cells permeates

https://doi.org/10.1038/s41567-022-01755-0

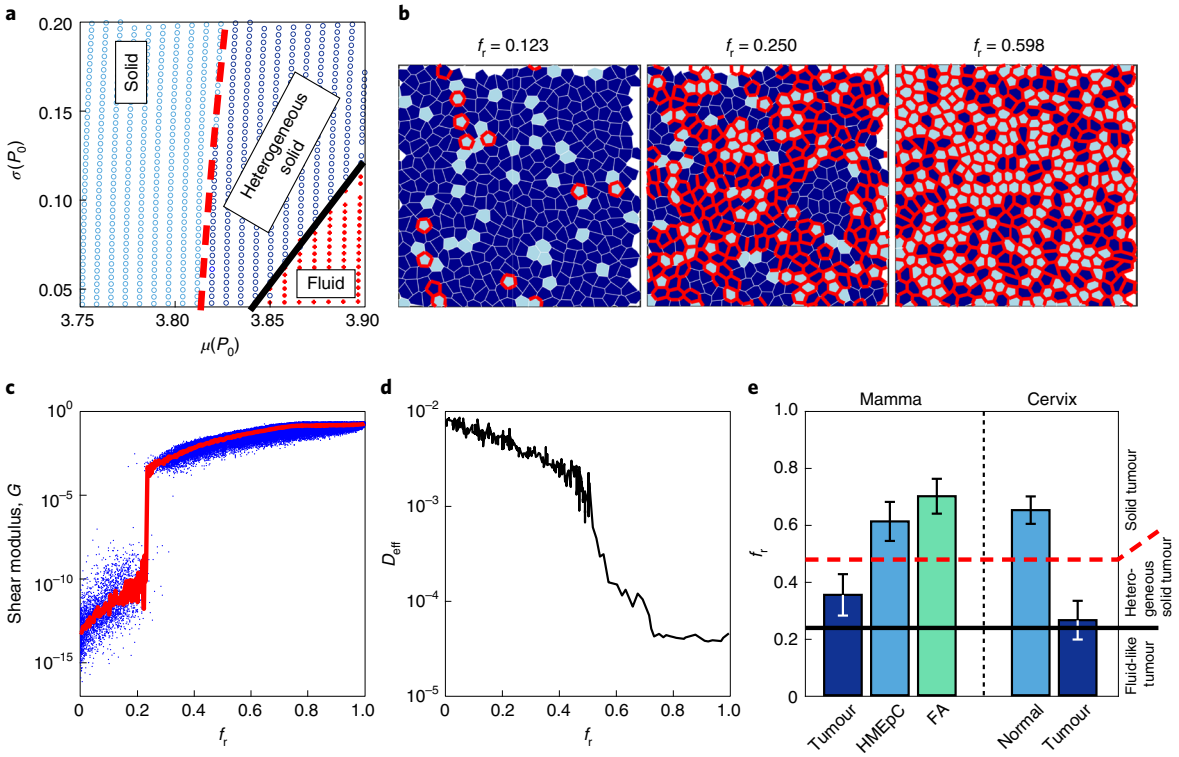

Fig. 5 | Two-dimensional vertex model simulations of mixtures of soft and rigid cancer cells. a, Mechanical phase diagram of cancer cell aggregates. This phase diagram distinguishes between solid, heterogeneous solid and fluid tissues as a function of the mean value of P_0 and its distribution width. The P_0 values of each cell are randomly assigned from a log-normal distribution. Here the fraction of rigid cells f_r is determined by mean(P_0) and s.d.(P_0). At $f_r = 0.24$, a rigidity transition occurs, which is indicated by the thick black line. Below $f_r = 0.24$, the tissue behaves as a fluid that lacks mechanical rigidity due to the absence of an intercellular tension network. Above $f_r = 0.24$, the tension network percolation generates solid behaviour despite the fact that no backbone of jammed, stiff cells spans the bulk. The red dashed curve represents the onset of contact percolation transition at $f_r = 0.48$ for stiff, jammed cells. The mismatch between rigidity and contact percolations results in an intermediate heterogeneous solid state as an unexpected mechanical state of tissues. The broad heterogeneity in cancer cells' mechanical properties is the key determinant of cellular tumour tissue. **b**, Representative snapshots of different mechanical states corresponding to fluid, heterogeneous solid and solid tissues. Rigid cancer cells are shown in light blue, whereas soft ones are in dark blue. The intercellular tension network is indicated by red lines drawn at cell junctions. The white space at the boundary is the cell-free space that arises from boundary conditions. **c**, Tumour rigidity is plotted as a function of the fraction of rigid cancer cells. The rigidity is expressed by the elastic shear modulus. The red curve represents the median of the scattered points at each f_r value and shows a rigidity transition at $f_r = 0.24$ from finite to vanishing shear modulus. **d**, Effective self-diffusivity as a function of f_r. Each cell has motility force $v_0 = 0.05$ and rotational noise $D_r = 1$. **e**, Fraction of rigid cells extracted from the relative deformations of various tissue types (Methods). This allows the mapping of each cell type to the categorization of tumour to the solid–fluid nexus as predicted by the vertex model. The error bars indicate 1 s.d.

the bulk, the tissue can spontaneously self-organize a spanning tension network that maintains rigidity. This heterogeneous solid phase explains how a tumour is able to simultaneously provide mechanical stability and cancer cell motility through the presence of soft, unjammed cells.

Soft cancer cells induce multicellular streaming

We use vital cancer cell tracking to confirm that there are both jammed islands and motile, unjammed areas in patient-derived tumour explants (12 cervix and 4 mamma carcinomas). In half the samples, we find unjammed as well as jammed regions in cancer clusters (examples in Fig. 6 and Supplementary Videos 1 and 2). The rigid jammed cancer cell clusters act as dynamic obstacles that lead to percolated tension networks and transiently channel soft, unjammed cells into parallel streams that wind through the cancer cell clusters (Fig. 6).

Our reductionist dynamic vertex model[45,57] makes obvious the effect of motile cells in a mechanically heterogeneous microenvironment. By calculating the velocity correlation between a motile cell and surrounding cells, we characterize the collective streaming behaviour (Fig. 6a–c). For a fluid state at $f_r = 0.12$, the correlations indicate that up to 3–4 other unjammed cancer cells tend to 'follow' the motile one. Lateral to the invading cell, the correlations are weaker and vanish at around a single-cell diameter. This directional anisotropy results in the formation of a cellular stream of cancer cells (Fig. 6d–f)[57]. The stream anisotropy decreases with f_r and disappears for the solid states at $f_r > 0.48$ (Extended Data Fig. 4). These results reveal that mechanical heterogeneity due to the presence of soft cancer cells has a strong tendency to enhance the collective stream-like behaviour, as found in our vital cancer cell tracking observations.

Heterogeneity allows solid tumours and motile cancer cells

Despite the fact that cancer is a systemic disease, particularly the fact that metastasis quintessentially depends on biomechanical changes at the cell and tissue level[59–61], the black-and-white characterization of tumour masses as stiff and cancer cells as soft demonstrates a lack of a comprehensive, detailed picture of mechanics in tumour biology. For the development of a malignant tumour, cancer cells have to move, proliferate and displace dense healthy tissue. Previously, the importance of cellular mechanical changes has been recognized when cancer cells leave the tumour cell mass and enter the surrounding stroma[25]. Cancer cell unjamming triggered by cell softening already boosts metastasis through a collective motility transition in cancer cell clusters within the tumour.

https://doi.org/10.1038/s41567-022-01755-0

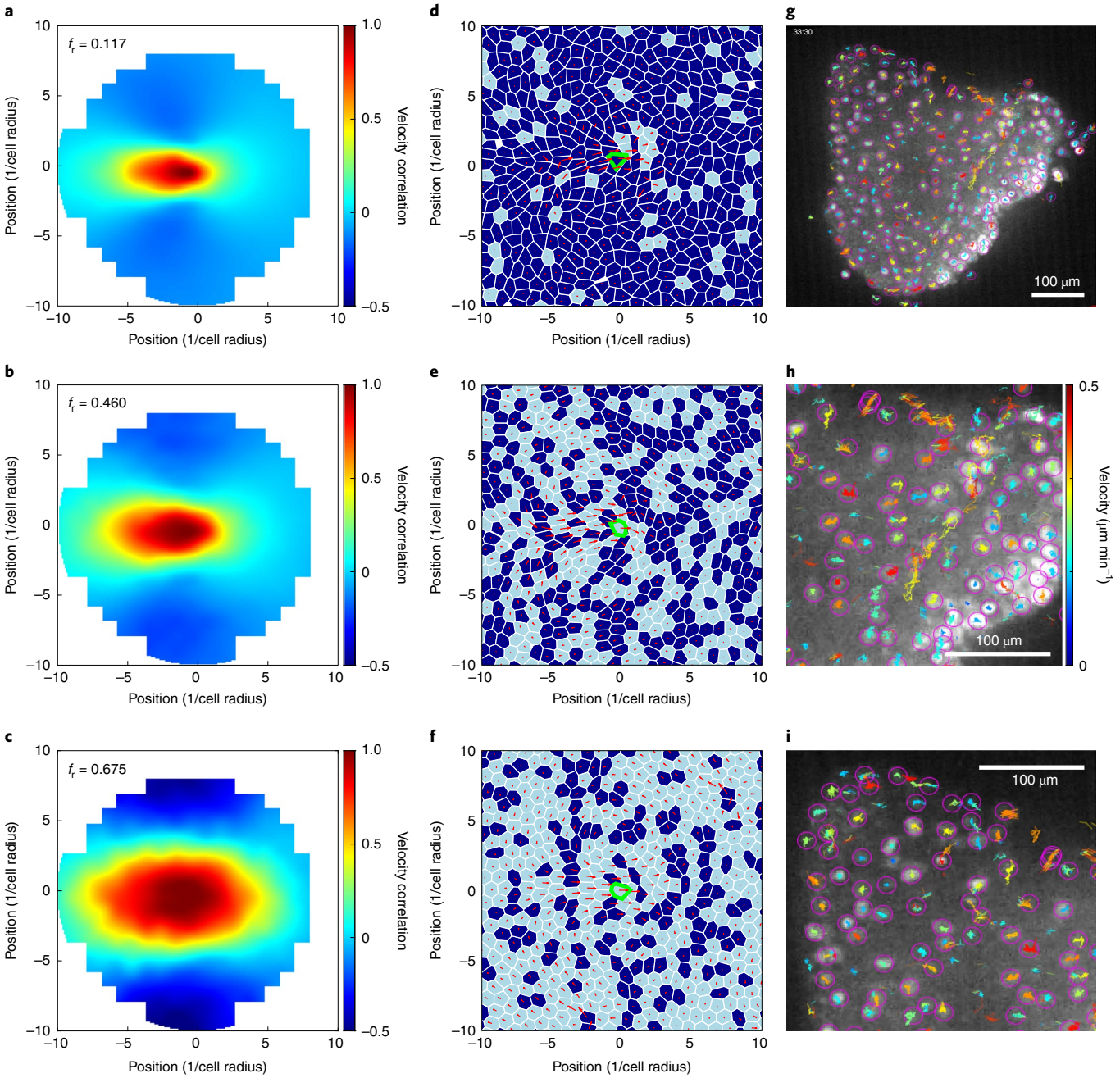

Fig. 6 | Emergent cellular stream caused by an invading cell inside a heterogeneous tumour. a–**c**, Simulated velocity correlations for fluid (**a**), heterogeneous solid (**b**) and solid (**c**) tissues. In the simulated $N = 400$ cell system, one actively invading cell, with propulsive force $v_0 = 0.4$ and rotational noise $D_r = 0.01$, is introduced (Methods). The colours indicate the value of correlations $C_{vv}(x, y)$ between the velocity vector of the invading cell and surrounding cells located at relative position (x, y). When $f_r = 0.1175$, directly behind the invading cell, the correlations are long ranged, indicating that up to 3–4 cells tend to 'follow' the invading cell. However, lateral to the invading cell, the correlations are weaker and decay beyond the one-cell diameter. This directional anisotropy is indicative of a cellular stream forming behind the invading cell. With increasing f_r, the anisotropy disappears. **d**–**f**, Snapshots of the cell velocity field taken from the corresponding states shown in **a** (**d**), **b** (**e**) and **c** (**f**). The invading cell is coloured with green edges. The light-blue and dark-blue colours represent rigid and soft cells, respectively. The red arrows show velocity. **g**, Tracks from time-lapse image series of a stream of cells in a cervical tumour sample ex vivo. A stream of cells is visible in the upper-right part of the piece (enlarged in **h**). The surrounding cells are immobile, that is, jammed (as shown in **i**). The cell nuclei are marked by purple circles. The tracks are coloured according to the maximal velocity, using the same colour scale in **g**–**i** (Supplementary Videos 1 and 2).

Cancer cells show a broad stiffness distribution shifted towards softer cells through deregulation. In cancer cell clusters, the softer cancer cells can squeeze by each other, which leads to collective cell streaming. With increasing stiffness, this becomes difficult and the cancer cells arrest through jamming. These collective mechanisms lead to jammed regions of stiff cells embedded in streams of soft cells. The rigid jammed islands feel each other by tension percolation through the surrounding fluid, unjammed areas, leading to a solid bulk behaviour. The resulting finite elastic storage modulus results in tumour stability and rigidity against external forces.

Multicellular streaming, which is frequently observed in the stroma surrounding the tumour[25,62,63], self-organizes collagen associated with the cellular cancer tissue into directed transport highways[64], further facilitating the aligned streaming. Streaming in the bulk of the

cell clusters causes a three-dimensional volume flow of cancer cells out of the depth of cancer cell clusters to the boundary, which is much more efficient than just the two-dimensional dissociation of cancer cells from the cluster surface. Moreover, multicellular streams exit the tumour with the ability to form collective clusters, enhancing their ability to survive outside the tumour mass and enhance metastatic cascade[65,66].

The emergent cooperative properties of a heterogeneous tissue induced by cancer cell softening cannot be understood by studying the molecular properties of single metastatic cells and may play a critical role in cancer invasiveness. The interplay of mechanical heterogeneity and cancer cell unjamming regulates the stiffness of cancer cell aggregates and simultaneously permits cell motility. To our knowledge, this property of the heterogeneous solid state goes beyond previously reported states of active matter. Deregulation and dedifferentiation as well as the spectrum of epithelial–mesenchymal transition, which are part of any malignant transformation, most probably cause a broad mechanical heterogeneity together with a shift to softer cells. Thus, we expect that the observed mechanical changes occur inherently with early neoplasm.

The ability for cancer cell unjamming may be part of the initial difference between benign tumours that grow locally and malignant, invasive tumours. To overcome the complexity and heterogeneity, the universal physics underlying the mechanical processes in the progression of solid tumours, which is agnostic to the molecular details of different tumour entities, may provide a more general perspective on cancer development as a systemic disease than the molecular cell perspective alone. Since the described processes relate to the initial steps of cancer cell spreading, they may become important predictors of patient outcome complementary to genetic signatures. As described here, pathological mechanical changes driven by emergent effects, which cannot be directly related to a simple molecular cause, are a missing link in understanding cancer and will ultimately lead to new diagnostics as well as therapy.

Online content

Any methods, additional references, Nature Research reporting summaries, source data, extended data, supplementary information, acknowledgements, peer review information; details of author contributions and competing interests; and statements of data and code availability are available at https://doi.org/10.1038/s41567-022-01755-0.

References

1. Friedman, E., Verderame, M., Winawer, S. & Pollack, R. Actin cytoskeletal organization loss in the benign-to-malignant tumor transition in cultured human colonic epithelial cells. *Cancer Res.* **44**, 3040–3050 (1984).
2. Cross, S. E., Jin, Y.-S., Rao, J. & Gimzewski, J. K. Nanomechanical analysis of cells from cancer patients. *Nat. Nanotechnol.* **2**, 780–783 (2007).
3. Lekka, M. et al. Elasticity of normal and cancerous human bladder cells studied by scanning force microscopy. *Eur. Biophys. J.* **28**, 312–316 (1999).
4. Guck, J., Ananthakrishnan, R., Moon, T. J., Cunningham, C. C. & Käs, J. Optical deformability of soft biological dielectrics. *Phys. Rev. Lett.* **84**, 5451–5454 (2000).
5. Tse, H. T. K. et al. Quantitative diagnosis of malignant pleural effusions by single-cell mechanophenotyping. *Sci. Transl. Med.* **5**, 212ra163 (2013).
6. Karantza, V. Keratins in health and cancer: more than mere epithelial cell markers. *Oncogene* **30**, 127–138 (2011).
7. Yang, J. et al. Guidelines and definitions for research on epithelial–mesenchymal transition. *Nat. Rev. Mol. Cell Biol.* **21**, 341–352 (2020).
8. Seltmann, K., Fritsch, A. W., Käs, J. A. & Magin, T. M. Keratins significantly contribute to cell stiffness and impact invasive behavior. *Proc. Natl Acad. Sci. USA* **110**, 18507–18512 (2013).
9. Friedl, P., Wolf, K. & Lammerding, J. Nuclear mechanics during cell migration. *Curr. Opin. Cell Biol.* **23**, 55–64 (2011).
10. Xia, Y., Pfeifer, C. R. & Discher, D. E. Nuclear mechanics during and after constricted migration. *Acta Mech. Sin.* **35**, 299–308 (2019).
11. Runge, J. et al. Evaluation of single-cell biomechanics as potential marker for oral squamous cell carcinomas: a pilot study. *Oral Dis.* **20**, e120–e127 (2014).
12. Nel, I., Morawetz, E. W., Tschodu, D., Käs, J. A. & Aktas, B. The mechanical fingerprint of circulating tumor cells (CTCs) in breast cancer patients. *Cancers* **13**, 1119 (2021).
13. Oktay, M. H. et al. Correlated immunohistochemical and cytological assays for the prediction of hematogenous dissemination of breast cancer. *J. Histochem. Cytochem.* **60**, 168–173 (2012).
14. Plodinec, M. et al. The nanomechanical signature of breast cancer. *Nat. Nanotechnol.* **7**, 757–765 (2012).
15. Grosser, S. et al. Cell and nucleus shape as an indicator of tissue fluidity in carcinoma. *Phys. Rev. X* **11**, 11033 (2021).
16. Helmlinger, G., Netti, P. A., Lichtenbeld, H. C., Melder, R. J. & Jain, R. K. Solid stress inhibits the growth of multicellular tumor spheroids. *Nat. Biotechnol.* **15**, 778–783 (1997).
17. Jonietz, E. Mechanics: the forces of cancer. *Nature* **491**, S56–S57 (2012).
18. Godard, B. G. & Heisenberg, C.-P. Cell division and tissue mechanics. *Curr. Opin. Cell Biol.* **60**, 114–120 (2019).
19. Ranft, J. et al. Fluidization of tissues by cell division and apoptosis. *Proc. Natl Acad. Sci. USA* **107**, 20863–20868 (2010).
20. Guevorkian, K., Colbert, M.-J., Durth, M., Dufour, S. & Brochard-Wyart, F. Aspiration of biological viscoelastic drops. *Phys. Rev. Lett.* **104**, 218101 (2010).
21. Pawlizak, S. et al. Testing the differential adhesion hypothesis across the epithelial–mesenchymal transition. *New J. Phys.* **17**, 83049 (2015).
22. Angelini, T. E. et al. Glass-like dynamics of collective cell migration. *Proc. Natl Acad. Sci. USA* **108**, 4714–4719 (2011).
23. Nnetu, K. D., Knorr, M., Käs, J. & Zink, M. The impact of jamming on boundaries of collectively moving weak-interacting cells. *New J. Phys.* **14**, 115012 (2012).
24. Collins, T. A., Yeoman, B. M. & Katira, P. To lead or to herd: optimal strategies for 3D collective migration of cell clusters. *Biomech. Model. Mechanobiol.* **19**, 1551–1564 (2020).
25. Ilina, O. et al. Cell–cell adhesion and 3D matrix confinement determine jamming transitions in breast cancer invasion. *Nat. Cell Biol.* **22**, 1103–1115 (2020).
26. Levental, K. R. et al. Matrix crosslinking forces tumor progression by enhancing integrin signaling. *Cell* **139**, 891–906 (2009).
27. Pickup, M. W., Mouw, J. K. & Weaver, V. M. The extracellular matrix modulates the hallmarks of cancer. *EMBO Rep.* **15**, 1243–1253 (2014).
28. Paszek, M. J. et al. Tensional homeostasis and the malignant phenotype. *Cancer Cell* **8**, 241–254 (2005).
29. DuFort, C. C., Paszek, M. J. & Weaver, V. M. Balancing forces: architectural control of mechanotransduction. *Nat. Rev. Mol. Cell Biol.* **12**, 308–319 (2011).
30. Raab, M. et al. Crawling from soft to stiff matrix polarizes the cytoskeleton and phosphoregulates myosin-II heavy chain. *J. Cell Biol.* **199**, 669–683 (2012).
31. Teixeira, M. R. & Heim, S. Cytogenetic analysis of tumor clonality. *Adv. Cancer Res.* **112**, 127–149 (2011).
32. Braun, J. et al. A compact 0.5 T MR elastography device and its application for studying viscoelasticity changes in biological tissues during progressive formalin fixation. *Magn. Reson. Med.* **79**, 470–478 (2018).

33. Sauer, F. et al. Whole tissue and single cell mechanics are correlated in human brain tumors. *Soft Matter* **17**, 10744–10752 (2021).
34. Sauer, F. et al. Collagen networks determine viscoelastic properties of connective tissues yet do not hinder diffusion of the aqueous solvent. *Soft Matter* **15**, 3055–3064 (2019).
35. Bonfanti, A., Kaplan, J. L., Charras, G. & Kabla, A. Fractional viscoelastic models for power-law materials. *Soft Matter* **16**, 6002–6020 (2020).
36. Wu, P.-H. et al. A comparison of methods to assess cell mechanical properties. *Nat. Methods* **15**, 491–498 (2018).
37. Jiang, X. et al. In vivo high-resolution magnetic resonance elastography of the uterine corpus and cervix. *Eur. Radiol.* **24**, 3025–3033 (2014).
38. Streitberger, K.-J. et al. How tissue fluidity influences brain tumor progression. *Proc. Natl Acad. Sci. USA* **117**, 128–134 (2020).
39. Hecht, F. M. et al. Imaging viscoelastic properties of live cells by AFM: power-law rheology on the nanoscale. *Soft Matter* **11**, 4584–4591 (2015).
40. Hiratsuka, S. et al. The number distribution of complex shear modulus of single cells measured by atomic force microscopy. *Ultramicroscopy* **109**, 937–941 (2009).
41. Guck, J. et al. The optical stretcher: a novel laser tool to micromanipulate cells. *Biophys. J.* **81**, 767–784 (2001).
42. Honda, H. Description of cellular patterns by Dirichlet domains: the two-dimensional case. *J. Theor. Biol.* **72**, 523–543 (1978).
43. Nagai, T. & Honda, H. A dynamic cell model for the formation of epithelial tissues. *Philos. Mag. B* **81**, 699–719 (2001).
44. Atia, L. et al. Geometric constraints during epithelial jamming. *Nat. Phys.* **14**, 613–620 (2018).
45. Mitchel, J. A. et al. In primary airway epithelial cells, the unjamming transition is distinct from the epithelial-to-mesenchymal transition. *Nat. Commun.* **11**, 5053 (2020).
46. Park, J.-A. et al. Unjamming and cell shape in the asthmatic airway epithelium. *Nat. Mater.* **14**, 1040–1048 (2015).
47. Honda, H. & Nagai, T. Cell models lead to understanding of multi-cellular morphogenesis consisting of successive self-construction of cells. *J. Biochem.* **157**, 129–136 (2015).
48. Blauth, E., Kubitschke, H., Gottheil, P., Grosser, S. & Käs, J. A. Jamming in embryogenesis and cancer progression. *Front. Phys.* **9**, 666709 (2021).
49. Li, X., Das, A. & Bi, D. Mechanical heterogeneity in tissues promotes rigidity and controls cellular invasion. *Phys. Rev. Lett.* **123**, 058101 (2019).
50. Amack, J. D. & Manning, M. L. Knowing the boundaries: extending the differential adhesion hypothesis in embryonic cell sorting. *Science* **338**, 212–215 (2012).
51. Sahu, P. et al. Small-scale demixing in confluent biological tissues. *Soft Matter* **16**, 3325–3337 (2020).
52. Huang, J., Cochran, J. O., Fielding, S. M., Marchetti, M. C. & Bi, D. Shear-driven solidification and nonlinear elasticity in epithelial tissues. *Phys. Rev. Lett.* **128**, 178001 (2022).
53. Labernadie, A. et al. A mechanically active heterotypic E-cadherin/N-cadherin adhesion enables fibroblasts to drive cancer cell invasion. *Nat. Cell Biol.* **19**, 224–237 (2017).
54. Merkel, M., Baumgarten, K., Tighe, B. P. & Manning, M. L. A minimal-length approach unifies rigidity in underconstrained materials. *Proc. Natl Acad. Sci. USA* **116**, 6560–6568 (2019).
55. Damavandi, O. K., Hagh, V. F., Santangelo, C. D. & Manning, M. L. Energetic rigidity. I. A unifying theory of mechanical stability. *Phys. Rev. E* **105**, 025003 (2022).
56. Yan, L. & Bi, D. Multicellular rosettes drive fluid-solid transition in epithelial tissues. *Phys. Rev. X* **9**, 011029 (2019).
57. Das, A., Sastry, S. & Bi, D. Controlled neighbor exchanges drive glassy behavior, intermittency, and cell streaming in epithelial tissues. *Phys. Rev. X* **11**, 041037 (2021).
58. Bi, D., Yang, X., Marchetti, M. C. & Manning, M. L. Motility-driven glass and jamming transitions in biological tissues. *Phys. Rev. X* **6**, 021011 (2016).
59. Mierke, C. T. The matrix environmental and cell mechanical properties regulate cell migration and contribute to the invasive phenotype of cancer cells. *Rep. Prog. Phys.* **82**, 064602 (2019).
60. Gensbittel, V. et al. Mechanical adaptability of tumor cells in metastasis. *Dev. Cell* **56**, 164–179 (2021).
61. Nia, H. T., Munn, L. L. & Jain, R. K. Physical traits of cancer. *Science* **370**, eaaz0868 (2020).
62. Greeley, C. F. & Frost, A. R. Cytologic features of ductal and lobular carcinoma in fine needle aspirates of the breast. *Acta Cytol.* **41**, 333–340 (1997).
63. Conklin, M. W. et al. Aligned collagen is a prognostic signature for survival in human breast carcinoma. *Am. J. Pathol.* **178**, 1221–1232 (2011).
64. Sharma, V. P. et al. SUN-MKL1 crosstalk regulates nuclear deformation and fast motility of breast carcinoma cells in fibrillar ECM microenvironment. *Cells* **10**, 1549 (2021).
65. Basan, M., Risler, T., Joanny, J.-F., Sastre-Garau, X. & Prost, J. Homeostatic competition drives tumor growth and metastasis nucleation. *HFSP J.* **3**, 265–272 (2009).
66. Liu, X. et al. Homophilic CD44 interactions mediate tumor cell aggregation and polyclonal metastasis in patient-derived breast cancer models. *Cancer Discov.* **9**, 96–113 (2019).

Methods

Experimental procedures

Ethics votum. This study was approved by the Ethics Committees of the Medical Faculty of Leipzig University for mamma and cervix carcinoma (090-10-19042010 and 227-10-23082010, respectively), and the Medical Association Hamburg for mamma samples. For the FA samples, the study was approved by the Institutional Review Board of the Montefiore Hospital (protocol no. 02-12-328). A consent document was signed by all the patients. Diagnostic-relevant parts of the tumour biopsy were used for standard tumour classification done by the responsible pathologists. All the patient samples were blinded and pathological staging was received after the evaluation of measurement data.

Primary tissue samples. The remaining tissue with vital cells were used for cancer cell extraction. To dissolve a tissue into individual cells, the tissue samples were sliced into pieces of about 1 mm thickness and put into a gentleMACS Unique C tube (Miltenyi Biotec) containing 5 ml Dulbecco's modified Eagle medium (DMEM)/Ham's F12 medium supplemented with either 1.60 mg ml^{-1} collagenase P (Roche) and 20 µg ml^{-1} DNAse for breast cancer samples or 0.25 mg ml^{-1} collagenase 1A (Sigma), 0.25 mg ml^{-1} pronase (Roche) and 20 µg ml^{-1} DNAse for cervical cancer samples. The C tubes were mounted onto the gentleMACS dissociator and stirred using a customized dissociation routine (that is, 30 s mixing at varying speeds). The suspension was then incubated at 37 °C for 30–60 min. This step was repeated twice until no tissue clusters were visible. The single-cell suspension was then centrifuged first at 40×*g* to collect the remaining cell clusters and cell debris. This was followed by another centrifuge step at 300×*g* for 5–10 min. The pellet containing the cells from the tumour sample was then resuspended and the cells were cultured first in DMEM/Ham's F12 supplemented with 10% foetal calf serum and ×1 penicillin/streptomycin/amphotericin B for 24 h; afterwards, a serum-free medium was used for culture (HuMEC medium (Gibco) for breast cancer cells and defined keratinocyte serum-free medium (Gibco) for cervical cancer cells, each supplemented with ×1 penicillin/streptomycin/amphotericin B). These media are optimized for epithelia cell culture and promote the growth of epithelia cells as well as suppress other cell types by the supplementation of growth factors and other components[67]. Fine-needle aspiration biopsy was used to obtain the samples from malignant breast tumours and FAs, a benign lesion of breast tissue. In contrast to core biopsy, where a small cylinder of tissue is obtained, a smaller needle (21 gauge) was used. By exerting a negative pressure, mainly loosely attached cells and sheets of epithelial cells were collected due to the capillary effect when inserted into FAs[68]. The obtained cells were shortly cultured as described above and all the vital cells were used for measurement. Primary human mamma epithelial cells (Invitrogen) and HMEpC (PromoCell) were cultured according to the protocols provided.

Biomechanical measurements of cancer cells using automated microfluidic OS. The OS is a two-beam laser trap, enabling biomechanical studies without physical contact[4,69]. Two opposing infrared laser beams form a stable trap. The suspended cells were injected and delivered through a microfluidic device to the centre of the trap. They were probed in a creep experiment where they were subjected to a step-stress profile, stretching with a high laser power for 2 s and holding for another 2 s with low power afterwards to observe their relaxation behaviour. The measurements were fully automated. Phase-contrast image sequences taken during the measurements were analysed using custom-made image analysis software to extract the time course of the observed relative cell deformation. The measured cells remain viable after stretching[70]. The applied laser power exerted a peak tensile stress of about 20 Pa on the cells causing an elongation of 0.5–7.0% of the cell diameter along the laser axis. Actively contracting cells can lead to an underestimation of deformation, but is more common in cancer cells (Supplementary Fig. 1); therefore, it might result in a slight underestimation of the difference. Log-normal distributions were fitted to the data and the significance was tested with the Mann–Whitney *U*-test (MWU test). The width of the distributions was characterized by the interquartile range with the difference between the first and third quartile.

Biomechanical measurements of cancer tissues using AFM. The tissue samples from breast and cervix carcinomas and adjacent healthy tissues were obtained during routine tumour resections. The tissue samples were measured within hours after resection. The tissue samples were chopped into 400-µm-thin slices with a McIlwain tissue chopper. Subsequently, the slices were glued (Histoacryl, B. Braun) onto microscope slides followed by the measurement of elastic strength (Young's modulus). The AFM used is a NanoWizard 4 instrument with 300 µm HybridStage (JPK) combined with an Axio Zoom.V16 instrument (ZEISS). A CONT (NanoWorld) contact-mode cantilever was modified with a 6-µm-diameter polystyrene bead to increase the contact area. The force ramps were recorded with the following parameters: maximum force, 7.5 nN; *z* speed, 20 µm s^{-1}; *z* length, 30 µm; capture rate, 2,048 Hz; imaging area, up to 1 × 1 mm^2 was split into smaller squares of 200–250 µm side length to fit into the piezo range of the hybrid stage. The maps were recorded with 10 µm data-point spacing. The AFM data were first analysed with the JPK data processing software (version 7.1.18) to calculate the Young's modulus using a Hertz fit to the smoothed and baseline-corrected force–indentation curves. The data were post-processed with a custom-written MATLAB program (MathWorks, version 2018b) to fit a log-normal distribution (2,000–10,000 data points per sample). The significance was tested with the MWU test. By using simultaneous fluorescence microscopy of DNA-stained cell nuclei, we assured that our maps, which we obtained, are from tumour areas with cancer cell clusters and not from the surrounding ECM.

Biomechanical measurements of single cells and MTS. MCF-10A and MDA-MB436 cells were cultured in cell culture flasks (TPP) for single-cell AFM measurements. Multicellular tumour spheroids (MTS) were formed on UltraPure agarose gels in a 96-well plate. Here 20,000 cells are added to each well, as they cannot adhere to the agarose; they adhere only to the other cells present and form the MTS. MDA-MB-436 cells were cultured in 90% DMEM (without sodium pyruvate), 10% foetal calf serum and 1% 10,000 U ml^{-1} penicillin/streptomycin. MCF-7 cells were cultured in 88% Eagle's minimal essential medium supplemented with 10 µg ml^{-1} insulin and 1 mM sodium pyruvate, 10% foetal calf serum/foetal bovine serum, 1% non-essential amino acids and 1% penicillin/streptomycin. The cells and MTS were measured with a CellHesion 200 instrument (JPK) and a tipless cantilever (Arrow TL1, NanoWorld). Single cells and MTS were directly measured after passaging into a Petri dish (TPP), and still being only weakly adherent to reduce the influence of the substrate. The CellHesion instrument is equipped with a custom climate chamber to provide 37 °C and 5% CO_2 during the measurements.

Biomechanical measurements of cancer tissues using MRE. Tabletop MRE measurements were carried out on 8 mm punch biopsies from the same tissues described earlier. The setup consists of a tabletop magnetic resonance imaging scanner (Pure Devices) with a 10 mm bore and 0.5 T permanent magnet that was customized by an additional gradient amplifier (DC-600, Pure Devices) and a piezoelectric driver controlled by a magnetic resonance imaging system (Piezosystem Jena) covering the frequency range between 200 and 6,000 Hz. The tissue samples were placed at the bottom of 7 mm glass tubes protected from evaporation by the addition of a cotton wool ball soaked in phosphate-buffered saline at the top of the tube and sealed by a plastic plug with a silicon shock absorber at the bottom and a single slice of polyvinyl chloride at the top. The glass tubes with the samples

were coupled from the top to the piezo driver and the section with the sample was positioned within the bore of the magnetic resonance imaging scanner, which was heated to 37 °C. The vibrations from the piezo actuator are constrained in axial motion and coupled via the glass walls into the sample. A detailed overview of the imaging sequences and motion-encoding gradients is described elsewhere[6]. In brief, the data acquisition time for each frequency was approximately 8 min; a frequency range of 1–6 kHz was covered in 500 Hz intervals, resulting in 11 measurement points and a total runtime of approximately 1.5 h. The following acquisition parameters were used: repetition time, 500 ms; echo time, 42 ms; slice thickness, 3.00 mm; matrix size, 56 × 56; field of view, 8.40 × 8.40 mm^2 resulting in a voxel size of 0.15 × 0.15 × 3.00 mm^3. The acquired data were unwrapped and Fourier transformed in time to extract complex-valued wave images for each driving frequency. The wave profiles for deflection parallel to the cylinder axis were created and fitted by the analytical solution of shear waves in a z-infinite cylinder[6], resulting in the complex wavenumber $k^* = k' + \mathrm{i}k''$. Based on the fact that the shear-wave speed c and shear-wave penetration rate a can be derived for each frequency, we get

$$c = \frac{2\pi f}{k'};\ a = \frac{f}{k''}. \tag{S1}$$

These parameters were directly fitted by a viscoelastic fractional element model to derive shear-modulus-related parameters.

$$G^* = \mu^{1-\alpha}\eta^{\alpha}\left(\mathrm{i}2\pi f\right)^{\alpha} \tag{S2}$$

Here μ and α are two independent variables; μ represents a measure of tissue stiffness and the power-law variable α is directly translated to the phase angle of the complex shear modulus G^* by multiplication with π/2. More details can be found elsewhere[32,34]. The KS test was used to check the significance.

Spheroid fusion experiments. Spheroids were formed with the same protocol as the AFM measurements. Two spheroids were transferred into a single well and observed with phase contrast microscopy over several hours. The used Leica DM IRB instrument was equipped with a custom climate chamber to provide 37 °C and 5% CO_2 during the measurement. Spheroids were fitted with two circles, the angle θ is the angle between the line connecting the two centre points and the radius from one centre to the intersection of the two circles. The progress of spheroid fusion was tracked over time and calculated as $\Delta(\cos\theta)/\Delta t$ in the time period of 24–36 h of fusion. The significance was checked with the KS test.

Vertex model of a mechanically heterogeneous tissue. We use the vertex model to understand the collective mechanical behaviour of dense tumour aggregates. In the vertex model, a two-dimensional confluent epithelial tissue is governed by the energy function[42,71–75] $E = \sum_{i=1}^{N}\left[K_A(A_i - A_0^i)^2 + K_P(P_i - P_0^i)^2\right]$ where cell areas $\{A_i\}$ and perimeters $\{P_i\}$ are functionals of the positions of vertices $\{\mathbf{r}_i\}$. Also, K_A and K_P are the area and perimeter elasticities, respectively. The quadratic term in A_i results from resistance to cell volume changes[71,73]. Changes to cell perimeters are related to the deformation of actomyosin cortex[71,73]. The term $K_P P_i^2$ corresponds to the energy cost of deforming the cortex. The linear term, $-2K_P P_0^i P_i$, is the effective line tension by cell i, which gives rise to a 'preferred perimeter' P_0^i. The value of P_0^i emerges from an interplay of cell–cell adhesion and cortical tension[71]. Here we assume the preferred cell area A_0 does not vary from cell to cell and is set to be the average area per cell ($A_0^i = \bar{A}$). The energy can be non-dimensionalized by choosing $K_P\bar{A}$ as the energy unit and $\sqrt{\bar{A}}$ as the length unit:

$$\varepsilon = \sum_{i=1}^{N}\left[\kappa_A(a_i - 1)^2 + (p_i - p_0^i)^2\right]$$

where $a_i = A_i/\bar{A}$ and $p_i = P_i/\sqrt{\bar{A}}$ are the rescaled area and perimeter of the ith cell, respectively. Also, $\kappa_A = K_A\bar{A}/K_P$ is the rescaled cell area elasticity and $p_0^i = P_0^i/\sqrt{\bar{A}}$ is the preferred cell shape index[76].

In this model, cell stiffness is determined by tension τ_m on cell–cell junctions (edges). For an edge with length l_m, the tension is given by[49,56,77]

$$\tau_m \equiv \frac{\partial \varepsilon}{\partial l_m} = (p_i - p_0^i) + (p_j - p_0^j),$$

where p_i and p_j are the rescaled perimeters of cells i and j, respectively, adjacent to edge m. As a result, cell stiffness is directly tuned by the preferred cell shape indices. To capture the experimental heterogeneities in single-cell stiffness and cell–cell interactions[14,78–80], we introduce variations in the preferred shape indices[49]. The majority of this work uses a log-normal distributed set of $\{p_0^i\}$. The results are insensitive to the form of distribution for $\{p_0^i\}$.

To initialize the simulation, Voronoi cells[58] are used to provide a set of initial vertex positions. Then, each cell is assigned a value of p_0 drawn from a log-normal distribution. The set of p_0 values remains as quenched variables. We use a combination of FIRE (fast inertial relaxation engine) and conjugate-gradient algorithms[81,82] to minimize the tissue energy under periodic boundary conditions with a fixed equilibrium cell area $A_0 = \bar{A} = 1$. This algorithm produces stable states where the net residual force on vertices is less than 10^{-8}. For this work, we simulate tissues with $N = 400$ cells. Each tissue is characterized by a mean (μ_{p0}) and s.d. (σ_{p0}) of single-cell p_0 values. We have systematically studied a large range of these parameters: $\mu_{p0} = 3.75$–3.90; $\sigma_{p0} = 0.05$ to −0.20. Following a previous theoretical study[49], we define the fraction of rigid cell f_r as the fraction of cells with $p_0 < 3.812$, which can be written as

$$f_r = \int_{-\infty}^{\mu^*} \mathcal{F}_{\mu,\sigma}(p_0)\,\mathrm{d}p_0.$$

Here $\mathcal{F}_{\mu,\sigma}(p_0)$ is the distribution function of p_0. For a log-normal-distributed p_0, the fraction of rigid cells is analytically given by

$$f_r = (1/2)\mathrm{erfc}[(\mu - \log(\mu^*))/(\sqrt{2}\sigma)].$$

Here erfc is the complementary error function and μ and σ are the control parameters of the log-normal distribution for which the mean and s.d. can be calculated as

$$\mu_{p_0} = \mathrm{e}^{\mu + \frac{\sigma^2}{2}}$$

$$\sigma_{p_0} = \left(\mathrm{e}^{\sigma^2} - 1\right)\mathrm{e}^{2\mu+\sigma^2}.$$

Calculating mechanical response at the tissue level. At the tissue level, its mechanical response is characterized by shear modulus G. A non-zero G corresponds to a solid-like tissue, whereas G vanishes for a fluid state. We obtain G by calculating the linear response to an infinitesimal affine strain γ via the Born–Huang formulation[83]

$$G = G_{\text{affine}} - G_{\text{non-affine}} = \frac{1}{A_{\text{total}}}\left[\frac{\partial^2 E}{\partial \gamma^2} - \Xi_{i\mu}M^{-1}_{i\mu j\nu}\Xi_{j\nu}\right]_{\gamma=0}.$$

In the above equation, $\Xi_{i\mu}$ is the derivative of the force on vertex i with respect to strain given by

$$\Xi_{i\mu} \equiv \frac{\partial^2 E}{\partial \gamma \partial r_{i\mu}},$$

where $r_{i\mu}$ is the position of vertex i and $\mu = x, y$ is the Cartesian index. Also, $A_{\text{total}} = \sum_i^N A_i$ is the total area of the tissue. Also, M is the Hessian

matrix given by the second derivative of tissue energy E with respect to position vectors of vertices i and j (refs. [49,56]):

$$M_{i\mu jv} = \frac{\partial^2 E}{\partial r_{i\mu}\partial r_{jv}}.$$

Using effective diffusivity to characterize dynamics of cell motion. We use self-diffusivity $D_s = \lim_{t\to\infty}\langle \Delta r(t)^2\rangle/(4t)$ to distinguish between the solid and fluid states[57], where $\lim_{t\to\infty}\langle \Delta r(t)^2\rangle$ is the mean square displacement. For practicality, we calculate D_s using simulation runs of 2×10^5 time steps at step size $\Delta t = 4\times10^{-2}$ using Euler's method with propulsive force $v_0 = 0.05$ and rotational noise of cells $D_r = 1$ under periodic boundaries. We present the self-diffusivity in units of $D_0 = v_0^2/(2D_r)$, which is the free-diffusion constant of an isolated cell. Then, $D_{eff} = D_s/D_0$ serves as a dynamical order parameter that distinguishes a fluid state from a solid state. The simulations are performed in the Surface Evolver program.

Accounting for measured distributions of cell stiffness. The experimental data for breast and cervix cancer cells are well described by log-normal distributions. The rigidity of the tissue with p_0 values given by these distributions can be obtained. We stress that only the relative cell stiffness can be inferred from the experimental data, but not the actual value of $=p_0$ for each cell. This is because p_0 is controlled by the interplay between cortical tension and cell–cell adhesion, whereas the OS only measures the mechanical tension, that is, the stiffness of the single-cell cortex in the absence of any cell–cell interactions. These data do not infer the effective tension that the cells experience in a confluent tissue. Nonetheless, this analysis provides an understanding of how soft cancer cells impact the mechanical behaviour of tissues. In particular, it suggests the possibility that a tumour—containing cells that are on average softer than that of the healthy tissue—could actually still exhibit rigidity at the collective tissue level due to the broadness of distribution.

The fraction of rigid cells can be extracted from the relative deformations of various tissue types. For each cell type, we use the mean deformation value of non-cancer cells (Fig. 3) to define the single-cell rigidity threshold for both non-cancer and cancer phenotypes. The f_r value for each cell type is then calculated by computing the fraction of cells with deformation values smaller than the mean deformation value of their non-cancer counterpart. This allows the mapping of each cell type in each tumour category to the solid–fluid nexus predicted within the theory.

Heterogeneity and cellular invasion. Here we use a dynamic vertex model[45] to simulate a tissue where only a single cell is invasive to study the effect of heterotypic cellular environment on cell migration. The invading cell has a propulsive force v_0 along a polarity vector $\hat{n}$, which undergoes random rotational diffusion[58] at a slow rate. This mimics the directional motility of a metastatic cell under the influence of strong chemotactic signals[84]. In the model, each vertex v evolves according to the overdamped equation of motion, with a viscous drag Γ as

$$\Gamma\frac{d\mathbf{r}_\mu}{dt} = \begin{cases} -\frac{\partial \epsilon}{\partial r_\mu} + v_0\hat{n} & \text{vertices of invading cell,} \\ -\frac{\partial \epsilon}{\partial r_\mu} & \text{for other vertices.} \end{cases}$$

The polarity vector undergoes random rotational diffusion as

$$\partial_t\theta_i = \eta_i(t)$$
$$\langle \eta_i(t)\eta_j(t')\rangle = 2D_r\delta(t-t')\delta_{ij},$$

where θ_i is the polarity angle that defines $\hat{n}$ and $\eta_i(t)$ is a white-noise process with zero mean and variance $2D_r$. The value of angular noise D_r determines the memory of stochastic noise in the system, giving rise to a persistence timescale $\tau = 1/D_r$ for the polarization vector $\hat{n}$. The timescale $\tau = 1/D_r$ controls the persistence of cell motion.

We numerically simulate the model using molecular dynamics by performing 10^5 integration steps at a step size of $\Delta t = 10^{-2}$ using Euler's method with propulsive force $v_0 = 0.4$ and rotational noise $D_r = 0.01$ for $N = 400$ cells under periodic boundaries. With heterogeneity, tissues in the range of $0 < f_r < 1$ become accessible and cells moving through them must interact with rigid as well as soft neighbouring cells along the path of invasion. This results in a highly intermittent migration dynamics for the invading cell.

Emergence of stream-like collective behaviour. To reveal the motility patterns in a heterogeneous tissue, we assume a log-normal distribution of p_0 values based on the broad distribution of cell deformations from the OS. Since cancer cells are also shown to be more contractile and the contractility mechanism is also responsible for cell traction, we assume that soft cells ($p_0 > 3.812$) have larger motility than rigid cells ($p_0 < 3.812$).

To analyse the motion of the invading cell, we always orient the invading cell such that its direction of motion is along the x axis, that is, we choose a frame of reference in which the invading cell is located at ($x = 0, y = 0$). To correlate the motion of the invading cell and other cells in its vicinity, we compute the correlation function as[23]

$$C_{vv}(x,y) = < v_{\text{active}} \cdot v(x,y) >,$$

Positions are in units of mean cell diameter. When $f_r = 0.11$, directly behind the invading cell, the correlations are long ranged indicating that up to 3–4 cells tend to 'follow' the invading cell. However, lateral to the invading cell, the correlations are weaker and decay beyond the one-cell diameter. This directional anisotropy is indicative of a cellular stream forming behind the invading cell. With an increase in f_r, the anisotropy disappears. To further quantify the behaviour of stream anisotropy with changing f_r, we calculate the correlation lengths ξ_x, ξ_y in the x and y directions, respectively, where the correlation $C_{vv}(x,y)$ decays to a threshold of 10^{-3}. Then, the stream anisotropy parameter is given by the ratio ξ_x/ξ_y and we plot it as a function of f_r (Supplementary Fig. 5).

Reporting summary

Further information on research design is available in the Nature Research Reporting Summary linked to this article.

Data availability

All data are available upon request from the corresponding author.

Code availability

Simulation data and code are available from D.B. (d.bi@northeastern.edu) on reasonable request.

References

67. Hammond, S. L., Ham, R. G. & Stampfer, M. R. Serum-free growth of human mammary epithelial cells: rapid clonal growth in defined medium and extended serial passage with pituitary extract. *Proc. Natl Acad. Sci. USA* **81**, 5435–5439 (1984).
68. Rosa, M., Mohammadi, A. & Masood, S. The value of fine needle aspiration biopsy in the diagnosis and prognostic assessment of palpable breast lesions. *Diagn. Cytopathol.* **40**, 26–34 (2012).
69. Lincoln, B., Wottawah, F., Schinkinger, S., Ebert, S. & Guck, J. High-throughput rheological measurements with an optical stretcher. *Methods Cell Biol.* **83**, 397–423 (2007).
70. Wetzel, F. et al. Single cell viability and impact of heating by laser absorption. *Eur. Biophys. J.* **40**, 1109–1114 (2011).
71. Farhadifar, R. et al. The influence of cell mechanics, cell-cell interactions, and proliferation on epithelial packing. *Curr. Biol.* **17**, 2095–2104 (2007).

72. Fletcher, A. G., Osterfield, M., Baker, R. E. & Shvartsman, S. Y. Vertex models of epithelial morphogenesis. *Biophys. J.* **106**, 2291–2304 (2014).
73. Staple, D. B. et al. Mechanics and remodelling of cell packings in epithelia. *Eur. Phys. J. E* **33**, 117–127 (2010).
74. Li, B. & Sun, S. X. Coherent motions in confluent cell monolayer sheets. *Biophys. J.* **107**, 1532–1541 (2014).
75. Hufnagel, L., Teleman, A. A., Rouault, H., Cohen, S. M. & Shraiman, B. I. On the mechanism of wing size determination in fly development. *Proc. Natl Acad. Sci. USA* **104**, 3835–3840 (2007).
76. Bi, D., Lopez, J. H., Schwarz, J. M. & Manning, M. L. A density-independent rigidity transition in biological tissues. *Nat. Phys.* **11**, 1074–1079 (2015).
77. Yang, X. et al. Correlating cell shape and cellular stress in motile confluent tissues. *Proc. Natl Acad. Sci. USA* **114**, 12663–12668 (2017).
78. Fujii, Y. et al. Spontaneous spatial correlation of elastic modulus in jammed epithelial monolayers observed by AFM. *Biophys. J.* **116**, 1152–1158 (2019).
79. Wu, D. et al. CD138-negative myeloma cells regulate mechanical properties of bone marrow stromal cells through SDF-1/CXCR4/AKT signaling pathway. *Biochim. Biophys. Acta* **1853**, 338–347 (2015).
80. Ciasca, G. et al. Nano-mechanical signature of brain tumours. *Nanoscale* **8**, 19629–19643 (2016).
81. Bitzek, E., Koskinen, P., Gähler, F., Moseler, M. & Gumbsch, P. Structural relaxation made simple. *Phys. Rev. Lett.* **97**, 170201 (2006).
82. Allen, M. P. & Tildesley, D. J. *Computer Simulation of Liquids* (Oxford Univ. Press, 2017).
83. Maloney, C. E. & Lemaître, A. Amorphous systems in athermal, quasistatic shear. *Phys. Rev. E* **74**, 016118 (2006).
84. Clark, A. G. & Vignjevic, D. M. Modes of cancer cell invasion and the role of the microenvironment. *Curr. Opin. Cell Biol.* **36**, 13–22 (2015).

Acknowledgements

We would like to thank A. Bruckert, J. Schnedemann and S. Klingkowski from Pathologie Hamburg-West, as well as F. Juliano from Montefiore Hospital, for the preparation of tissue samples. This work was funded by the German Science Foundation (DFG; KA1116/9-1 and KA1116/17-1), as well as project 'FORCE' within the EU's Horizon 2020 research and innovation programme. Graduate students A.W.F., T.R.K., S.P. and F.W. were funded by fellowships of the DFG Excellence graduate school BuildMoNa. The research with A.N. was part of the joint project EXPRIMAGE funded by the German Federal Ministry for Education and Research (BMBF 13N9366). T.F. was funded by ERC Advanced Grant 'HoldCancerBack' (741350). D.B. and X.L. would like to acknowledge support from the Northeastern University TIER 1 Grant, National Science Foundation DMR-2046683; the Alfred P. Sloan Foundation; MathWorks Microgrants; and the Northeastern University Discovery Cluster. M.H.O. and J.C. were funded by CA255153. We would also like to acknowledge the Syracuse University HTC Campus Grid, NSF award ACI-1341006.

Author contributions

J.A.K. planned and directed this study. T.F., D.B., X.L. and J.A.K. wrote the manuscript. All the authors discussed the results and commented on the manuscript. F.W. carried out experiments on the breast tumour cells and controls. A.W.F. and S.P. were responsible for the measurements of cervical samples. R.S., T.R.K., S.P., A.W.F., E.M. and F.W. developed a sample preparation and measurement routine. T.F., M.Z. and S.F. carried out the AFM measurements. F.S. carried out the MRE measurements. J.B. provided technical support for the MRE measurements. S.G. and J.L. performed the experiments on MTS. F.R. performed the experiments on tumour explants. B.A., L.-C.H., M.H., K.B., S.B., B.W., M.H.O., J.C. and A.N. provided the patient samples and scientific/medical advice for data interpretation. D.B., X.L., M.C.M. and M.L.M designed the theoretical and simulation models. D.B., X.L. and M.L.M. developed, executed and analysed the simulation results with oversight from J.A.K.

Competing interests

The authors have no competing interests.

Additional information

Extended data is available for this paper at https://doi.org/10.1038/s41567-022-01755-0.

Supplementary information The online version contains supplementary material available at https://doi.org/10.1038/s41567-022-01755-0.

Correspondence and requests for materials should be addressed to Josef A. Käs.

Peer review information *Nature Physics* thanks Dennis Discher, Sanjay Kumar and the other, anonymous, reviewer(s) for their contribution to the peer review of this work.

Reprints and permissions information is available at www.nature.com/reprints.

https://doi.org/10.1038/s41567-022-01755-0

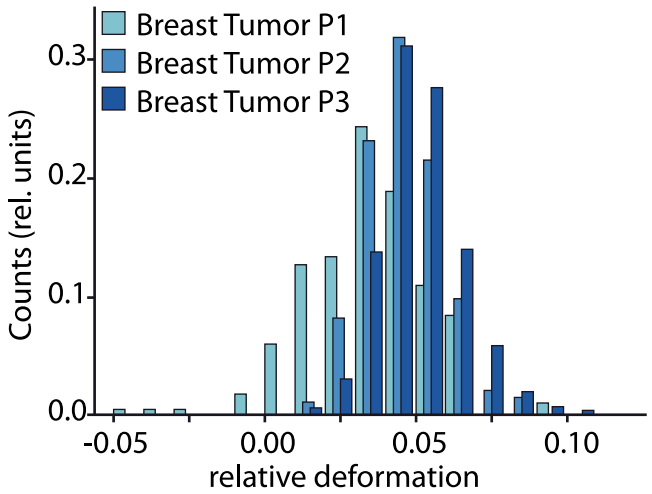

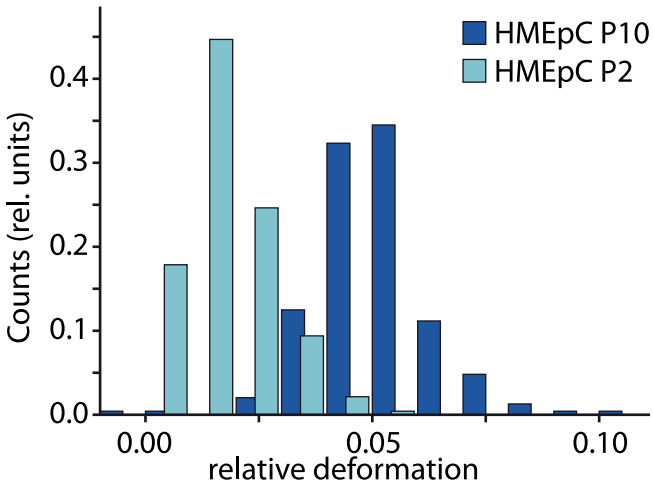

Extended Data Fig. 1 | Effect of passaging on the deformability of primary breast tumour and normal epithelial cells. Left) Distribution of the maximum relative cell deformations (observed at t = 3 s) for a breast cancer sample stretched at the end of passage number 1-3 (sample size: P1 = 164 cells, P 2 = 496 cells, P3 = 309 cells). Right) Relative deformation distribution epithelial cells from breast reduction (HMEpC) stretched at the end of passage number 2 and 10 (sample size: P2 = 352 cells, P10 = 702 cells). With increasing passage number more and more deformable cells are found. Time between passaging was 7 to 10 days.

https://doi.org/10.1038/s41567-022-01755-0

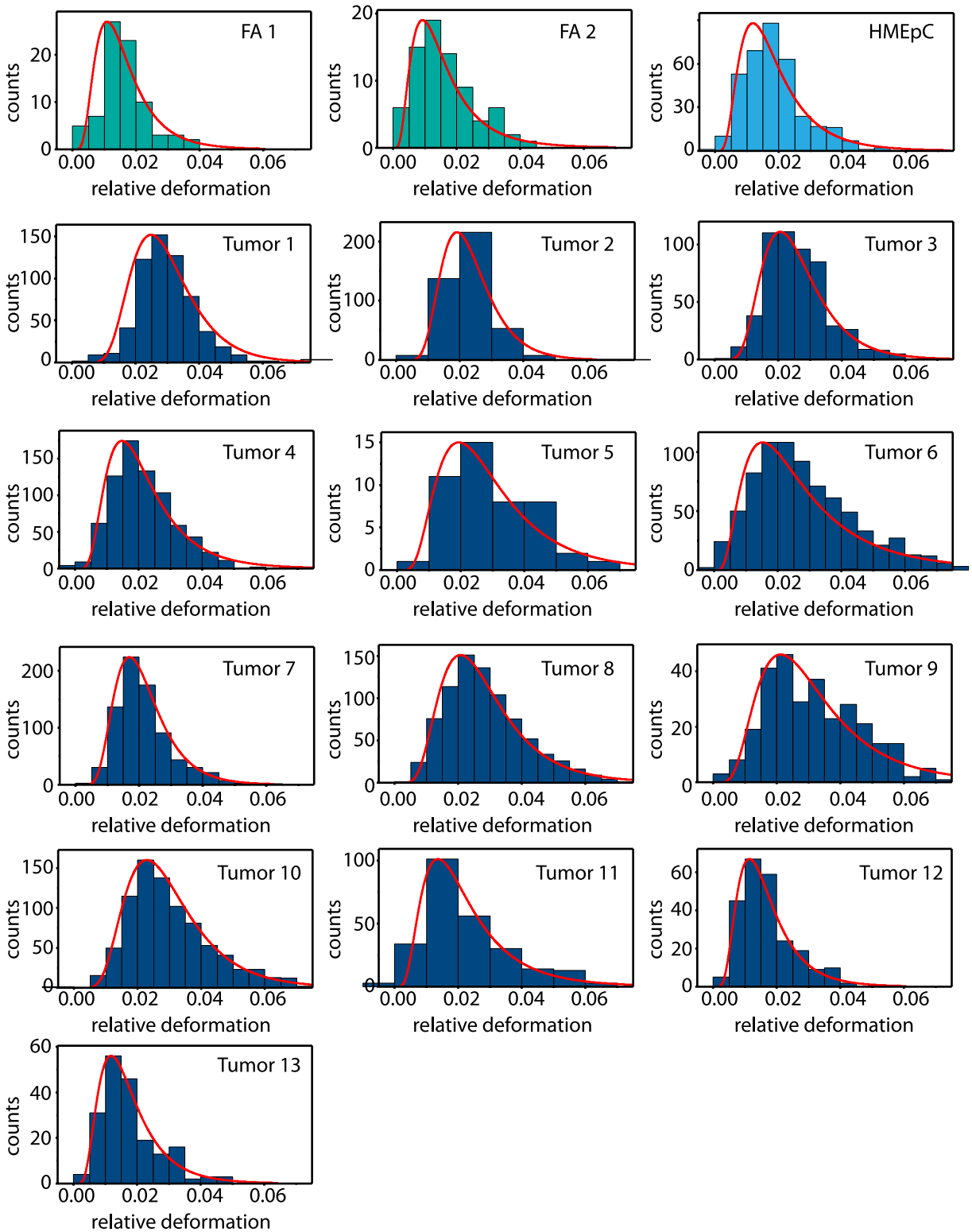

Extended Data Fig. 2 | Individual Histograms of the relative deformation of breast tumour samples. Cells isolated from 13 breast tumours were measured in the optical stretcher, 2 fibroadenomas (FA) and HMEpC cells serve as control. Log-Normal distributions were fitted to the histograms; details of the fits can be found in Extended Data Table 1.

https://doi.org/10.1038/s41567-022-01755-0

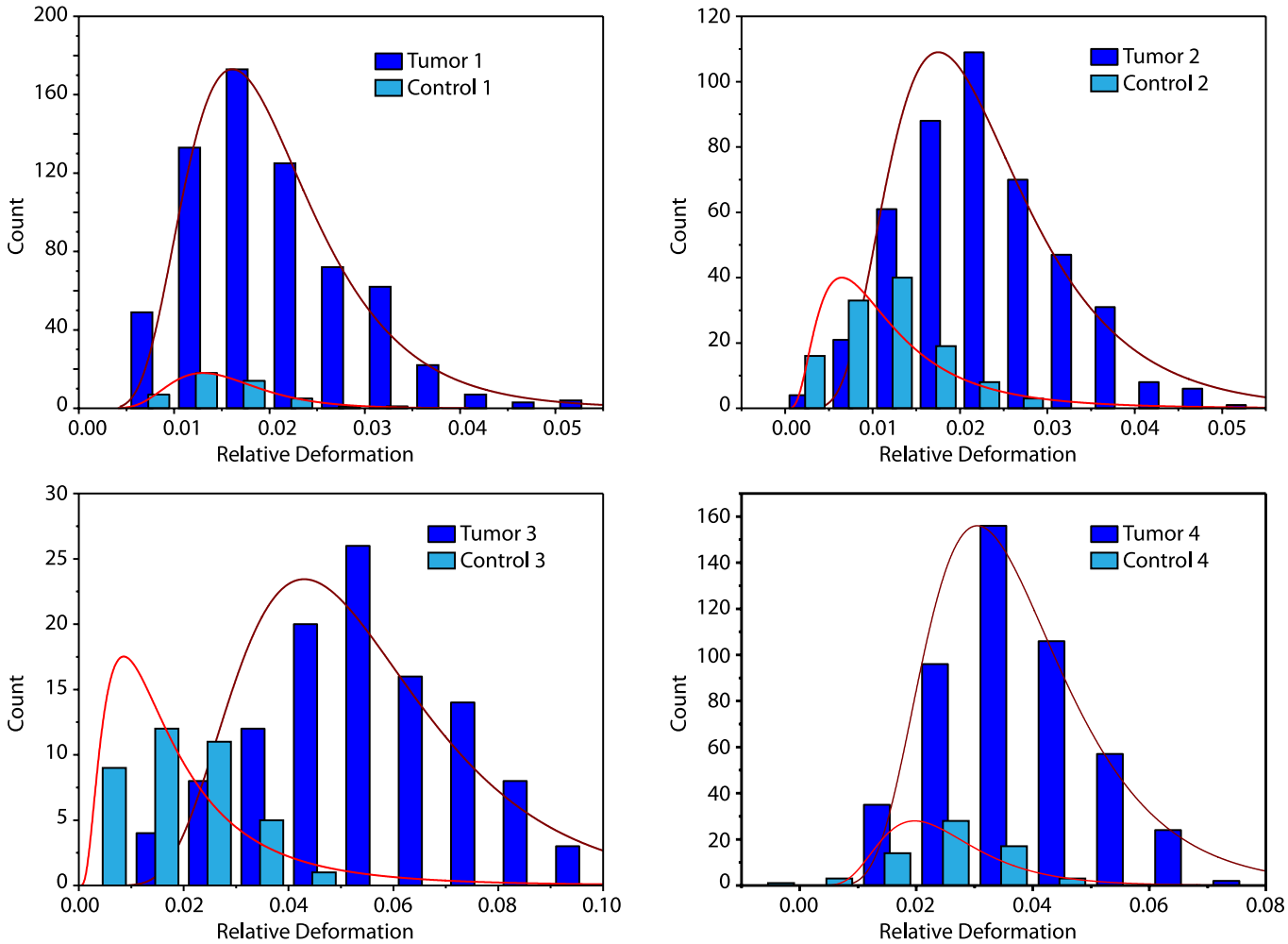

Extended Data Fig. 3 | Individual Histograms the relative deformation of Cervix Tumours. Cells were isolated from 4 cervix tumours and normal cervix tissue from the same patient as control. Log-Normal distributions were fitted; details of the fits can be found in Extended Data Table 1.

https://doi.org/10.1038/s41567-022-01755-0

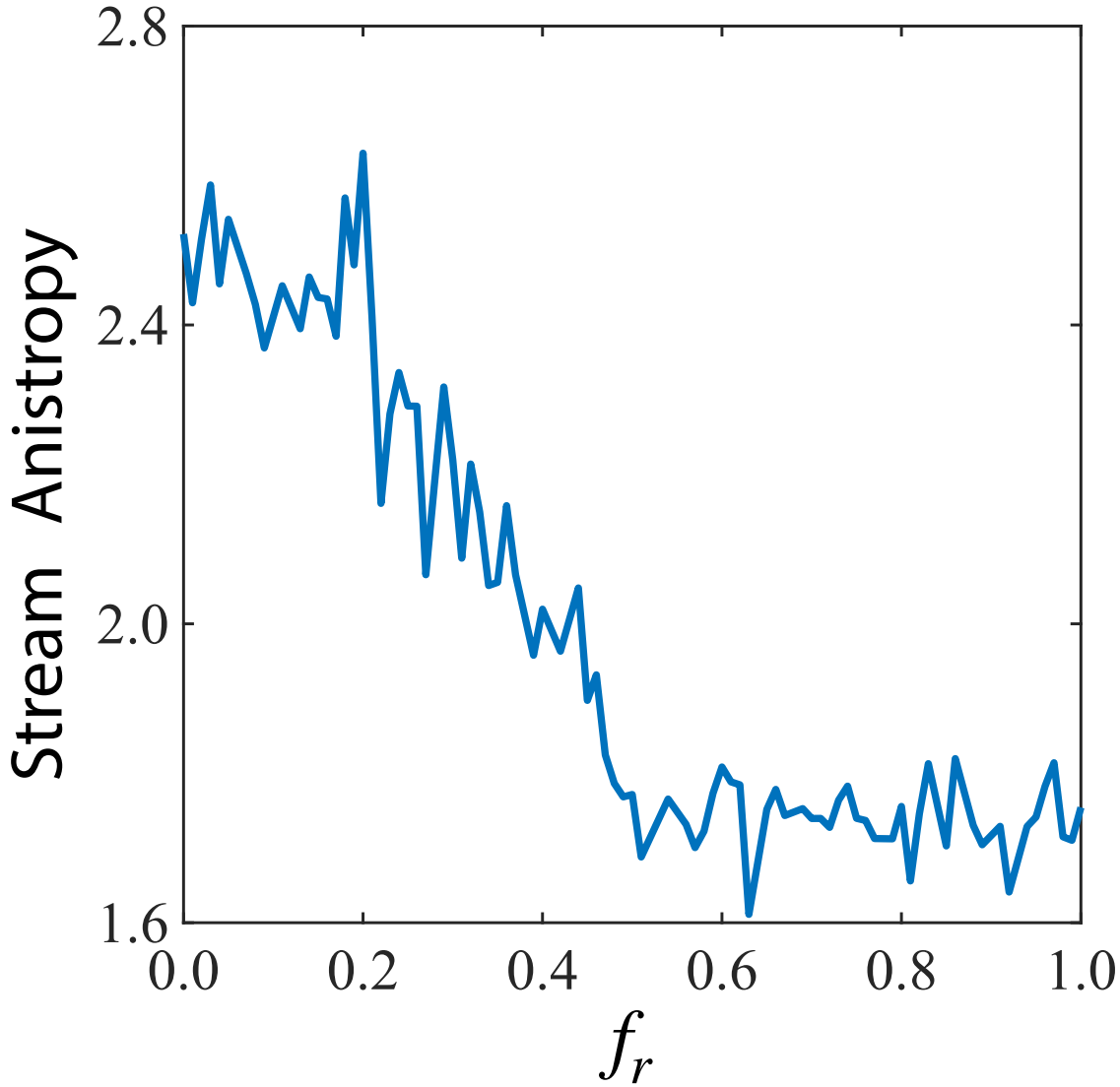

Extended Data Fig. 4 | The stream anisotropy as a function of f_r for the invading cell. The stream anisotropy as a function of f_r for the invading cell.

https://doi.org/10.1038/s41567-022-01755-0

Extended Data Table 1 | Statistic quantities of the tumour samples

sample	1st Quartile	Median	3rd Quartile	Inter-quartile (Q3 - Q1)	Log-Normal μ	Log-Normal σ	Grade (G), nodal metastasis (N+/N-)	T class (pT)	ER (x/12)	PR (x/12)	Her2 neu	additional	Age	sample size
Breast														
HMEpC	0,01162	0,01772	0,02306	0,01144	-4.121	0.563	cells from breast reduction, 2nd passage						23	352
FA 1	0,01145	0,01553	0,01981	0,00836	-4.245	0.527	fibroadenoma							80
FA 2	0,00935	0,01312	0,02051	0,01116	-4.299	0.622	fibroadenoma							76
Breast tumor 1	0.02388	0.02913	0.03485	0.01097	-3.571	0.353	3+	2	12	6	1+		>50	613
Breast tumor 2	0.01833	0.02279	0.02686	0.00853	-3.823	0.366	3-	1c	12	12	0		>50	423
Breast tumor 3	0.01899	0.02475	0.03142	0.01243	-3.725	0.399	3-	2	12	4	1+		>50	529
Breast tumor 4	0.01456	0.02004	0.02730	0.01274	-3.947	0.521	3-	2	0	0	1+	neoadjuv.	<50	750
Breast tumor 5	0.01913	0.02654	0.03923	0.02010	-3.651	0.542	2	1c	12	9	0		>50	46
Breast tumor 6	0.01661	0.02526	0.03768	0.02108	-3.746	0.666	3+	2	8	4	1+		>50	763
Breast tumor 7	0.01561	0.01974	0.02520	0.00959	-3.919	0.401	3+	3	8	4	2+		>50	770
Breast tumor 8	0.01939	0.02665	0.03564	0.01625	-3.661	0.465	3+	1	0	0	1+		>50	823
Breast tumor 9	0.02030	0.02998	0.04254	0.02224	-3.574	0.528	3-	2	6	6	1+		>50	291
Breast tumor 10	0.02119	0.02779	0.03743	0.01624	-3.590	0.434	3-	1	12	0	1+		>50	830
Breast tumor 11	0.01299	0.01884	0.02910	0.01611	-3.952	0.589	1	2	12	0	1+		>50	254
Breast tumor 12	0.01057	0.01514	0.02075	0.01018	-4.212	0.514	3-	2	8	6	0		<50	240
Breast tumor 13	0.01182	0.01551	0.02149	0.00966	-4.168	0,520	1	1c	12	12	0		<50	193
Cervix														
Cervix 1-t	0.01459	0.01888	0.02522	0.01063	-3.961	0.481	3 (N+)	2b				squamous	53	650
Cervix 1-n	0.01149	0.01458	0.01934	0.00785	-4.557	0.772	normal					cell ca.		46
Cervix 2-t	0.01661	0.02246	0.02880	0.01219	-3.857	0.434	3 (N+)	2b				adeno-	54	446
Cervix 2-n	0.00811	0.01164	0.01515	0.00704	-4.602	0.661	normal					carcinoma		119
Cervix 3-t	0.04179	0.05475	0.06730	0.02551	-2.983	0.405	2 (N-)	1b1				adeno-	55	111
Cervix 3-n	0.01038	0.01815	0.02579	0.01541	-4.185	0.758	normal					carcinoma		38
Cervix 4-t	0.02883	0.03669	0.04645	0.01763	-3.347	0.380	3(N-)	1b2				squamous	40	478
Cervix 4-n	0.01872	0.02434	0.03092	0.01220	-3.763	0.404	normal					cell ca.		66

nature portfolio

Corresponding author(s): Josef A. Käs

Last updated by author(s): Jul 13, 2022

Reporting Summary

Nature Portfolio wishes to improve the reproducibility of the work that we publish. This form provides structure for consistency and transparency in reporting. For further information on Nature Portfolio policies, see our Editorial Policies and the Editorial Policy Checklist.

Statistics

For all statistical analyses, confirm that the following items are present in the figure legend, table legend, main text, or Methods section.

n/a	Confirmed
☐	☒ The exact sample size (*n*) for each experimental group/condition, given as a discrete number and unit of measurement
☐	☒ A statement on whether measurements were taken from distinct samples or whether the same sample was measured repeatedly
☐	☒ The statistical test(s) used AND whether they are one- or two-sided *Only common tests should be described solely by name; describe more complex techniques in the Methods section.*
☐	☒ A description of all covariates tested
☐	☒ A description of any assumptions or corrections, such as tests of normality and adjustment for multiple comparisons
☐	☒ A full description of the statistical parameters including central tendency (e.g. means) or other basic estimates (e.g. regression coefficient) AND variation (e.g. standard deviation) or associated estimates of uncertainty (e.g. confidence intervals)
☐	☒ For null hypothesis testing, the test statistic (e.g. *F*, *t*, *r*) with confidence intervals, effect sizes, degrees of freedom and *P* value noted *Give P values as exact values whenever suitable.*
☒	☐ For Bayesian analysis, information on the choice of priors and Markov chain Monte Carlo settings
☒	☐ For hierarchical and complex designs, identification of the appropriate level for tests and full reporting of outcomes
☒	☐ Estimates of effect sizes (e.g. Cohen's *d*, Pearson's *r*), indicating how they were calculated

Our web collection on statistics for biologists contains articles on many of the points above.

Software and code

Policy information about availability of computer code

Data collection	Experimental data was recorded with the manufactures software on comercially available instruments.
Data analysis	Data was analysed with MATLAB (R2021a), and Origin (2017G).

For manuscripts utilizing custom algorithms or software that are central to the research but not yet described in published literature, software must be made available to editors and reviewers. We strongly encourage code deposition in a community repository (e.g. GitHub). See the Nature Portfolio guidelines for submitting code & software for further information.

Data

Policy information about availability of data

All manuscripts must include a data availability statement. This statement should provide the following information, where applicable:

- Accession codes, unique identifiers, or web links for publicly available datasets
- A description of any restrictions on data availability
- For clinical datasets or third party data, please ensure that the statement adheres to our policy

All data are available upon request from the corresponding author. Simulation data and code is available from Dapeng Bi, Department of Physics, Northeastern University, Boston, MA 02115, USA d.bi@northeastern.edu

Human research participants

Policy information about studies involving human research participants and Sex and Gender in Research.

Reporting on sex and gender	Due to the nature of the tumours investigated only tissue from female patients was used.
Population characteristics	*Describe the covariate-relevant population characteristics of the human research participants (e.g. age, genotypic information, past and current diagnosis and treatment categories). If you filled out the behavioural & social sciences study design questions and have nothing to add here, write "See above."*
Recruitment	Patients were recruited during routine cancer treatment.
Ethics oversight	ethics committees of the Medical Faculty of Leipzig Universit; medical association Hamburg; institutional review board of the Montefiore Hospital, Bronx, NY

Note that full information on the approval of the study protocol must also be provided in the manuscript.

Field-specific reporting

Please select the one below that is the best fit for your research. If you are not sure, read the appropriate sections before making your selection.

☒ Life sciences ☐ Behavioural & social sciences ☐ Ecological, evolutionary & environmental sciences

For a reference copy of the document with all sections, see nature.com/documents/nr-reporting-summary-flat.pdf

Life sciences study design

All studies must disclose on these points even when the disclosure is negative.

Sample size	*Describe how sample size was determined, detailing any statistical methods used to predetermine sample size OR if no sample-size calculation was performed, describe how sample sizes were chosen and provide a rationale for why these sample sizes are sufficient.*
Data exclusions	*Describe any data exclusions. If no data were excluded from the analyses, state so OR if data were excluded, describe the exclusions and the rationale behind them, indicating whether exclusion criteria were pre-established.*
Replication	*Describe the measures taken to verify the reproducibility of the experimental findings. If all attempts at replication were successful, confirm this OR if there are any findings that were not replicated or cannot be reproduced, note this and describe why.*
Randomization	*Describe how samples/organisms/participants were allocated into experimental groups. If allocation was not random, describe how covariates were controlled OR if this is not relevant to your study, explain why.*
Blinding	All patient samples were blinded and pathological staging was received after evaluation of the measurement data.

Reporting for specific materials, systems and methods

We require information from authors about some types of materials, experimental systems and methods used in many studies. Here, indicate whether each material, system or method listed is relevant to your study. If you are not sure if a list item applies to your research, read the appropriate section before selecting a response.

Materials & experimental systems

n/a	Involved in the study
☐	☐ Antibodies
☐	☒ Eukaryotic cell lines
☐	☐ Palaeontology and archaeology
☐	☐ Animals and other organisms
☐	☒ Clinical data
☐	☐ Dual use research of concern

Methods

n/a	Involved in the study
☐	☐ ChIP-seq
☐	☐ Flow cytometry
☐	☐ MRI-based neuroimaging

Antibodies

Antibodies used: *Describe all antibodies used in the study; as applicable, provide supplier name, catalog number, clone name, and lot number.*

Validation: *Describe the validation of each primary antibody for the species and application, noting any validation statements on the manufacturer's website, relevant citations, antibody profiles in online databases, or data provided in the manuscript.*

Eukaryotic cell lines

Policy information about cell lines and Sex and Gender in Research

Cell line source(s): Primary human mamma epithelial cells HMEC (Invitrogen)
HMEpC (PromoCell, Heidelberg)
MCF-10A, ATCC
MDA-MB-436, ATCC

Authentication: *Describe the authentication procedures for each cell line used OR declare that none of the cell lines used were authenticated.*

Mycoplasma contamination: *Confirm that all cell lines tested negative for mycoplasma contamination OR describe the results of the testing for mycoplasma contamination OR declare that the cell lines were not tested for mycoplasma contamination.*

Commonly misidentified lines (See ICLAC register): *Name any commonly misidentified cell lines used in the study and provide a rationale for their use.*

Palaeontology and Archaeology

Specimen provenance: *Provide provenance information for specimens and describe permits that were obtained for the work (including the name of the issuing authority, the date of issue, and any identifying information). Permits should encompass collection and, where applicable, export.*

Specimen deposition: *Indicate where the specimens have been deposited to permit free access by other researchers.*

Dating methods: *If new dates are provided, describe how they were obtained (e.g. collection, storage, sample pretreatment and measurement), where they were obtained (i.e. lab name), the calibration program and the protocol for quality assurance OR state that no new dates are provided.*

☐ Tick this box to confirm that the raw and calibrated dates are available in the paper or in Supplementary Information.

Ethics oversight: *Identify the organization(s) that approved or provided guidance on the study protocol, OR state that no ethical approval or guidance was required and explain why not.*

Note that full information on the approval of the study protocol must also be provided in the manuscript.

Animals and other research organisms

Policy information about studies involving animals; ARRIVE guidelines recommended for reporting animal research, and Sex and Gender in Research

Laboratory animals: *For laboratory animals, report species, strain and age OR state that the study did not involve laboratory animals.*

Wild animals: *Provide details on animals observed in or captured in the field; report species and age where possible. Describe how animals were caught and transported and what happened to captive animals after the study (if killed, explain why and describe method; if released, say where and when) OR state that the study did not involve wild animals.*

Reporting on sex: *Indicate if findings apply to only one sex; describe whether sex was considered in study design, methods used for assigning sex. Provide data disaggregated for sex where this information has been collected in the source data as appropriate; provide overall numbers in this Reporting Summary. Please state if this information has not been collected. Report sex-based analyses where performed, justify reasons for lack of sex-based analysis.*

Field-collected samples: *For laboratory work with field-collected samples, describe all relevant parameters such as housing, maintenance, temperature, photoperiod and end-of-experiment protocol OR state that the study did not involve samples collected from the field.*

Ethics oversight: *Identify the organization(s) that approved or provided guidance on the study protocol, OR state that no ethical approval or guidance was required and explain why not.*

Note that full information on the approval of the study protocol must also be provided in the manuscript.

Clinical data

Policy information about clinical studies

All manuscripts should comply with the ICMJE guidelines for publication of clinical research and a completed CONSORT checklist must be included with all submissions.

Clinical trial registration	This study was approved by the ethics committees of the Medical Faculty of Leipzig University for mamma and cervix carcinoma 090-10-19042010 and 227-10-23082010 (mamma and cervix), and the medical association Hamburg for mamma samples, and for fibroadenoma samples the study was approved by the institutional review board of the Montefiore Hospital, Bronx, NY IRB Protocol #: 02-12-328.
Study protocol	*Note where the full trial protocol can be accessed OR if not available, explain why.*
Data collection	*Describe the settings and locales of data collection, noting the time periods of recruitment and data collection.*
Outcomes	*Describe how you pre-defined primary and secondary outcome measures and how you assessed these measures.*

Dual use research of concern

Policy information about dual use research of concern

Hazards

Could the accidental, deliberate or reckless misuse of agents or technologies generated in the work, or the application of information presented in the manuscript, pose a threat to:

No	Yes	
☒	☐	Public health
☒	☐	National security
☒	☐	Crops and/or livestock
☒	☐	Ecosystems
☒	☐	Any other significant area

Experiments of concern

Does the work involve any of these experiments of concern:

No	Yes	
☒	☐	Demonstrate how to render a vaccine ineffective
☒	☐	Confer resistance to therapeutically useful antibiotics or antiviral agents
☒	☐	Enhance the virulence of a pathogen or render a nonpathogen virulent
☒	☐	Increase transmissibility of a pathogen
☒	☐	Alter the host range of a pathogen
☒	☐	Enable evasion of diagnostic/detection modalities
☒	☐	Enable the weaponization of a biological agent or toxin
☒	☐	Any other potentially harmful combination of experiments and agents

ChIP-seq

Data deposition

☐ Confirm that both raw and final processed data have been deposited in a public database such as GEO.

☐ Confirm that you have deposited or provided access to graph files (e.g. BED files) for the called peaks.

Data access links *May remain private before publication.*	*For "Initial submission" or "Revised version" documents, provide reviewer access links. For your "Final submission" document, provide a link to the deposited data.*
Files in database submission	*Provide a list of all files available in the database submission.*
Genome browser session (e.g. UCSC)	*Provide a link to an anonymized genome browser session for "Initial submission" and "Revised version" documents only, to enable peer review. Write "no longer applicable" for "Final submission" documents.*

Methodology

Replicates	*Describe the experimental replicates, specifying number, type and replicate agreement.*

Sequencing depth	*Describe the sequencing depth for each experiment, providing the total number of reads, uniquely mapped reads, length of reads and whether they were paired- or single-end.*
Antibodies	*Describe the antibodies used for the ChIP-seq experiments; as applicable, provide supplier name, catalog number, clone name, and lot number.*
Peak calling parameters	*Specify the command line program and parameters used for read mapping and peak calling, including the ChIP, control and index files used.*
Data quality	*Describe the methods used to ensure data quality in full detail, including how many peaks are at FDR 5% and above 5-fold enrichment.*
Software	*Describe the software used to collect and analyze the ChIP-seq data. For custom code that has been deposited into a community repository, provide accession details.*

Flow Cytometry

Plots

Confirm that:

☐ The axis labels state the marker and fluorochrome used (e.g. CD4-FITC).

☐ The axis scales are clearly visible. Include numbers along axes only for bottom left plot of group (a 'group' is an analysis of identical markers).

☐ All plots are contour plots with outliers or pseudocolor plots.

☐ A numerical value for number of cells or percentage (with statistics) is provided.

Methodology

Sample preparation	*Describe the sample preparation, detailing the biological source of the cells and any tissue processing steps used.*
Instrument	*Identify the instrument used for data collection, specifying make and model number.*
Software	*Describe the software used to collect and analyze the flow cytometry data. For custom code that has been deposited into a community repository, provide accession details.*
Cell population abundance	*Describe the abundance of the relevant cell populations within post-sort fractions, providing details on the purity of the samples and how it was determined.*
Gating strategy	*Describe the gating strategy used for all relevant experiments, specifying the preliminary FSC/SSC gates of the starting cell population, indicating where boundaries between "positive" and "negative" staining cell populations are defined.*

☐ Tick this box to confirm that a figure exemplifying the gating strategy is provided in the Supplementary Information.

Magnetic resonance imaging

Experimental design

Design type	*Indicate task or resting state; event-related or block design.*
Design specifications	*Specify the number of blocks, trials or experimental units per session and/or subject, and specify the length of each trial or block (if trials are blocked) and interval between trials.*
Behavioral performance measures	*State number and/or type of variables recorded (e.g. correct button press, response time) and what statistics were used to establish that the subjects were performing the task as expected (e.g. mean, range, and/or standard deviation across subjects).*

Acquisition

Imaging type(s)	*Specify: functional, structural, diffusion, perfusion.*
Field strength	*Specify in Tesla*
Sequence & imaging parameters	*Specify the pulse sequence type (gradient echo, spin echo, etc.), imaging type (EPI, spiral, etc.), field of view, matrix size, slice thickness, orientation and TE/TR/flip angle.*
Area of acquisition	*State whether a whole brain scan was used OR define the area of acquisition, describing how the region was determined.*

Diffusion MRI ☐ Used ☐ Not used

Preprocessing

Preprocessing software
Provide detail on software version and revision number and on specific parameters (model/functions, brain extraction, segmentation, smoothing kernel size, etc.).

Normalization
If data were normalized/standardized, describe the approach(es): specify linear or non-linear and define image types used for transformation OR indicate that data were not normalized and explain rationale for lack of normalization.

Normalization template
Describe the template used for normalization/transformation, specifying subject space or group standardized space (e.g. original Talairach, MNI305, ICBM152) OR indicate that the data were not normalized.

Noise and artifact removal
Describe your procedure(s) for artifact and structured noise removal, specifying motion parameters, tissue signals and physiological signals (heart rate, respiration).

Volume censoring
Define your software and/or method and criteria for volume censoring, and state the extent of such censoring.

Statistical modeling & inference

Model type and settings
Specify type (mass univariate, multivariate, RSA, predictive, etc.) and describe essential details of the model at the first and second levels (e.g. fixed, random or mixed effects; drift or auto-correlation).

Effect(s) tested
Define precise effect in terms of the task or stimulus conditions instead of psychological concepts and indicate whether ANOVA or factorial designs were used.

Specify type of analysis: ☐ Whole brain ☐ ROI-based ☐ Both

Statistic type for inference
(See Eklund et al. 2016)
Specify voxel-wise or cluster-wise and report all relevant parameters for cluster-wise methods.

Correction
Describe the type of correction and how it is obtained for multiple comparisons (e.g. FWE, FDR, permutation or Monte Carlo).

Models & analysis

n/a	Involved in the study
☐	☐ Functional and/or effective connectivity
☐	☐ Graph analysis
☐	☐ Multivariate modeling or predictive analysis

Functional and/or effective connectivity
Report the measures of dependence used and the model details (e.g. Pearson correlation, partial correlation, mutual information).

Graph analysis
Report the dependent variable and connectivity measure, specifying weighted graph or binarized graph, subject- or group-level, and the global and/or node summaries used (e.g. clustering coefficient, efficiency, etc.).

Multivariate modeling and predictive analysis
Specify independent variables, features extraction and dimension reduction, model, training and evaluation metrics.